Delayed Oligodendrocyte Progenitor Cell Recruitment and Maturation in Large Volume Demyelination

James J. M. Cooper[1], Jessie J. Polanco[2], Darpan Saraswat[1], Jennifer Peirick[3], Fraser J. Sim[1,2]

Department of Pharmacology and Toxicology[1], Neuroscience Program[2], Lab Animal Facilities[3], Jacobs School of Medicine and Biomedical Sciences, University at Buffalo, Buffalo, NY.

Address correspondence to:
Fraser Sim, Ph.D.
Department of Pharmacology and Toxicology
Jacobs School of Medicine and Biomedical Sciences
University at Buffalo
955 Main Street
Buffalo, NY 14203
716-829-2151
fjsim@buffalo.edu

Keywords: demyelination, remyelination, oligodendrocyte progenitor.

Running title: Oligodendrocyte progenitors and large volume demyelination

Abstract, 278; Introduction, 742; Discussion, 1491; Tables: 0, Figures: 8

Acknowledgements: This work was supported by NINDS grant (R01NS104021), National Multiple Sclerosis Society (RG-1701-26750), the Kalec Multiple Sclerosis Foundation, the Change MS Foundation. JJP received additional support from NIGMS (R25GM09545902), NCATS (UL1TR001412-S1), and New York State Department of Health (Empire State Stem Cell Fund) through the Stem Cells in Regenerative Medicine Fellowship (NYSTEM C30290GG). We acknowledge support provided by the Center for Computational Research at the University at Buffalo for use of the academic compute cluster for training the Keras-based convolution network.

Conflict of Interest: The authors declare no competing financial interests.

Abstract

Remyelination-inducing therapies have the potential to restore neurologic function and prevent progression in multiple sclerosis (MS). However, preclinical therapies capable of driving oligodendrocyte differentiation and enhancing remyelination in murine models have not yet yielded meaningful clinical improvement. These setbacks suggest that small animal models may be inadequate for the development and identification of promising regenerative therapies. Unlike MS, rodent models of demyelination undergo highly efficient remyelination, have typically very small volumes and exhibit abundant oligodendrocyte recruitment rapidly following demyelination. We hypothesized that oligodendrocyte progenitor cell (OPC) recruitment becomes rate-limiting as lesion volume increases leading to a failure of oligodendrocyte differentiation and endogenous remyelination. In this study, we utilized lysolecithin injection into the large white matter tracts of the rabbit to create demyelinated lesions that have cross-sectional areas 20-fold larger than those previously reported in mice, and volumes 8-fold larger. Unlike rodent lesions which show robust supernumerary OPC recruitment (representing a 3-10 fold increase in Olig2^{+} cell density), recruitment in the rabbit never exceeds normal levels. Importantly, the density of mature CC1^{+} oligodendrocytes failed to return to NAWM levels by 56 dpl and the percentage of differentiated oligodendrocytes drastically lagged behind that of rodent lesions. These results suggest that as lesion volume increases the requirement for increased OPC proliferation and migration becomes limiting. As oligodendrocyte differentiation from human OPCs is dependent on the local density of progenitors, the reduced density of progenitors in large lesions may contribute to failed differentiation and remyelination. Together, we show that large volume demyelination in the white matter of the rabbit recapitulates several key features of human MS lesions, and represents an important preclinical model for the assessment of remyelination therapies in human demyelinating disease.

INTRODUCTION

Primary demyelination is most commonly associated with multiple sclerosis (MS), where half of patients will require walking assistance after a decade of disease duration [1]. Immune-mediated demyelination and loss of oligodendrocytes (OL) results in loss of neurological function. In experimental models, remyelination relies on restoration of the OL population through the recruitment (both migration and proliferation) and subsequent differentiation and maturation of oligodendrocyte precursor cells (OPCs) [2]. OPCs are a multipotent stem cell population that are distributed throughout the adult CNS. While the role of adult OPCs in normal brain remains elusive, OPCs are responsible for the replacement of lost OLs in the context of demyelination [3]. Following a demyelinating event, OPCs migrate into the damaged region from adjacent healthy tissue where they become activated [4] and begin to proliferate. The expression of activation markers, such as Sox2, are downregulated as OPCs begin to differentiate and mature [4]. Newly generated OLs engage and ensheath denuded axons and upregulate myelin proteins resulting in the production of a thin myelin sheath with shorter internodes that is capable of restoring saltatory conduction and neurological function [5].

While remyelination is a common feature of early relapsing-remitting MS, remyelination failure becomes more common with increasing disease duration and age. Remyelination failure is thought to be due to the malfunction of one or more stages of oligodendrocyte regeneration: namely OPC recruitment, differentiation, and myelin formation [2]. While quiescent OPCs are associated with chronic demyelination in MS [6], the prevailing theory is that remyelination fails in MS due to a failure of differentiation. In response, a number of drug candidates aimed at boosting endogenous remyelination through the promotion of OPC differentiation have been developed and advanced to clinical trials after successful preclinical results, notably opicinumab (anti-Lingo1) and clemastine [7-9]. Unfortunately, while both were able to significantly improve visual evoked potential latency indicative of remyelination in the optic nerve, neither was able to significantly impact clinical outcome or imaging endpoints in initial trials [10-12]. The paradoxical success of differentiation-promoting therapies in rodent models, but little success in clinical trials suggests fundamental differences in the rate-limiting steps between remyelination in animal models and human MS.

In rodent models of demyelination, there is little evidence that the rate of OPC recruitment is rate-limiting. For example, when the number of OPCs within the lesion is experimentally increased via overexpression of PDGF-A there is no change in the time course or extent of remyelination [13]. Additionally, relatively few rounds of division are required to restore OPC density in rodent lesions (1-3 cycles) [14], and when nearly all OPCs are pharmacogenetically depleted in

92 the rodent brain OPC densities are restored in less than 10 days [15]. Indeed, it is only after long-
93 term administration of cuprizone to chronically deplete of OPCs over the period of several months
94 that recruitment fails and remyelination is inefficient [16]. As OPCs are recruited from the adjacent
95 NAWM, the burden of both migration and proliferation disproportionately increases with increased
96 lesion volume. In MS, individual demyelinating lesions have volumes of several thousand cubic
97 millimeters [17]. In contrast, the volume of focal demyelinated lesions modelled in rodents is very
98 small, typically less than 1 mm^3 [18, 19]. Thus, we hypothesized that OPC recruitment becomes rate-
99 limiting as lesion volume increases leading to a failure of OL differentiation and endogenous
100 remyelination.
101 In this study we sought to develop a model that more accurately recapitulates the burden
102 of recruitment seen in MS lesions. To do this we utilized the large white matter tracks of the rabbit
103 to create demyelinating lesions with cross-sectional areas 20 times that produced in mice. Along
104 with increased lesion size, OPC recruitment was substantially inferior to corresponding rodent
105 models and closely resembled the pattern observed in MS. Large volume rabbit lesions exhibited
106 distinct regional differences in the pattern of gliotic response, axonal injury, OPC recruitment,
107 activation and proliferation that evolved with time following induction of demyelination. Together,
108 we describe lysolecithin-induced lesions in the rabbit that recapitulate several key features of
109 demyelination in MS which may more accurately predict the outcome of novel remyelination-
110 inducing therapies in clinical trials.
111

112 **MATERIALS AND METHODS**

113 *Animals and surgery*

114 All experiments were performed according to protocols approved by the University at
115 Buffalo's Institutional Animal Care and Use Committee. New Zealand White Rabbits were
116 purchased as needed (Female, average weight 2.96 ± 0.13 kg and average age 15.79 ± 0.53
117 weeks) (Charles Rivers Laboratories, Wilmington, MA). Induction anesthesia was accomplished
118 via intramuscular injection of ketamine (35 mg/kg) and xylazine (5 mg/kg) into epaxial muscles.
119 After loss of consciousness, supplemental heating began and corneas were lubricated. The
120 proximal 3 cm of the tail was shaved to provide an optimal location for the pulse oximetry probe
121 (far preferable to use of ear or tongue). ECG leads and rectal temperature probe were placed.
122 After pre-oxygenation via face mask, rabbits were intubated in ventral recumbency with heads
123 and necks held in extension. A size 3.0 endotracheal tube was threaded over an 8-French urinary
124 catheter. After placement of the catheter through the glottis, the ET tube was advanced over the
125 catheter and into the trachea. Successful intubation was verified via immediate capnography.
126 Upon success, isoflurane was delivered via Bain Circuit (1-3%). An IV catheter was placed
127 (marginal ear vein), and the surgical site was shaved and prepped prior to moving the rabbit to
128 the operating room (OR). Pre-emptive, initial analgesics were administered (0.05 mg/kg
129 buprenorphine, subcutaneously (SC) and 1.5 mg/kg carprofen, SC).
130 Once moved onto the OR table, rabbits were immediately reconnected to isoflurane to ensure a
131 suitable anesthetic plane. Then, they were transiently disconnected from the Bain Circuit to allow
132 loose movement of the head into the stereotaxic frame (Kopf Model 902 Small Animal Stereotaxic
133 Instrument + Kopf Model 1240 Rabbit Adaptor + Rabbit Risers, Kopf Instruments, Tujunga, CA).
134 The endotracheal (ET) tube, was carefully moved to rest between the arms of the Kopf Rabbit
135 Adaptor. It was important that the ET tube was not advanced beyond 12 cm to avoid bronchial
136 obstruction. Once positioned, the capnograph and Bain Circuit were quickly reconnected. At this
137 time further careful positioning of the rabbit's head was possible via tooth bar, zygoma clamps
138 and nose clamp. General anesthesia could be maintained for the remainder of the stereotaxic
139 procedure with isoflurane. Spontaneous respirations were augmented by manual intermittent
140 positive pressure ventilations (IPPV). 0.1 mL bupivacaine (0.25%) or lidocaine (2%, diluted 1:1
141 with 0.9% NaCl) was injected SC. A 7-8 cm incision was made alone the midline of the scalp to
142 expose both bregma (intersection of the sagittal and coronal sutures) and lambda (intersection of
143 the sagittal and lambdoid sutures). Both left and right arm Hamilton needles were filled with
144 distilled H_2O to prevent occlusion and ensure flow prior to lysolecithin loading. Placing the needles
145 point on either bregma or lambda, the dorsal-ventral (DV) relationship was adjusted using the

146 Kopf Rabbit Adaptor until bregma was 1.5 mm above lambda. The arms of the Kopf frame were
147 adjusted to a 20° angle, and the needle points were placed on bregma. The anterior-posterior
148 (AP), lateral-medial (LM), and DV of each arm was recorded. The following adjustments were
149 made to these values: AP= +0.5 mm, LM= +7.7 mm, DV= -5.7 mm. Injection site was confirmed
150 via Evans Blue injection (**Supplemental Figure 3A**).Drill bits (Burrs for Micro Drill 19007-29, 2.9
151 mm, Foster City, CA) were sterilized via dry micro bead bench side sterilizer for 1 minute and
152 cooled with room temp saline. In advance of drilling, topical articaine (4%) was dripped onto the
153 skull and allowed to absorb and dry over drilling skull sites. Drill holes were made through the
154 skull to the level of the meninges with constant saline stream to prevent parenchymal heat
155 damage. A 30G needle was then used to puncture the meninges to allow for free passage of the
156 Hamilton needle. 1% lysolecithin was then injected at a rate 0.1 µl/min, with 5 minute wait times
157 between microliters to allow for diffusion. Once injection was completed, the needles were left in
158 place for 20 additional minutes to allow for diffusion.
159 Post-operatively, buprenorphine was administered (0.05 mg/kg, SC) 4 hours after the initial dose,
160 and carprofen (1.5 mg/kg, SC) was continued twice daily for a total of 4 consecutive days. Rabbits
161 were monitored daily after surgery and assessed for: mentation, weight loss from baseline,
162 appetite, water consumption, amount and character of feces, amount of urination, and presence
163 of neurologic signs. Post-surgical weight loss peaked at 28 dpl, followed by a rapid recovery
164 (**Supplemental Figure 3B-C**).

165 *Tissue processing*

166 Animals were sacrificed at 7, 14, 21, and 56 days post-lesion (dpl) by transcardial
167 perfusion of saline followed by 4% paraformaldehyde under deep anesthesia. Following
168 decapitation, whole brain tissue was extracted and post-fixed for 30 minutes in 4%
169 paraformaldehyde. For cryopreservation, the tissue was first left in 1x PBS overnight, then
170 transferred into a 7.5% sucrose solution overnight, and finally 15% sucrose overnight.
171 Cryoprotected tissue was then frozen in optimal cutting temperature medium (Tissue-Tek). Serial,
172 16 µm-thick coronal sections were cut using a Leica cryostat, and stored in -80 °C freezer until
173 processing.
174 To identify lesion location and volume, every 10th section was washed with 1x PBST (x3
175 by 5 min), stained with FloroMyelin for 1 hour at room temperature (1:300, Thermo Fisher
176 Scientific) and 4′,6-Diamidino-2-phenylindole dihydrochloride (DAPI) for 3 minutes (1:5000,
177 Sigma Aldrich), and mounted in prolong gold (Thermo Fisher Scientific). Lesions were identified
178 as regions with lesser FloroMyelin signal and corresponding hypercellularity by DAPI, compared

179 to surrounding white matter. Cross-sectional lesion areas were calculated for both left and right
180 hemisphere lesions using the NIH ImageJ software, and the largest cross-sectional area for each
181 lesion was identified as the lesion center.

182 *Estimation of lesion volume*

183 Lesion volume was calculated from the measured cross-sectional areas determined by
184 FloroMyelin staining using Cavalieri's estimator of morphometric volume [56]:
185

186 $$V_c = d\left(\sum_{i=0}^{n}(y_i)\right) - (t)y_{MAX}$$

187

188 Where V_c is the Cavalieri's estimated volume, d is the distance between sections, y_i is the cross-
189 sectional area of section i, t is the thickness of the sections, and y_{MAX} is the largest cross-
190 sectional area of the lesion. Since every 10th section was stained, $d = 160$ μm, and $t = 16$ μm.

191 *Immunohistochemistry (IHC)*

192 Slides immediately adjacent to the lesion centers, identified by FloroMyelin staining, were
193 used for all immunohistochemical procedures. In general, sections were permeabilized for 1 hour
194 with 1% Triton X-100 (Alfa Aesar) and 0.25% Tween 20 (Calbiochem). Sections were blocked for
195 1 hour with a solution containing 0.5% Triton X-100, 5% bovine serum albumin (BSA), and 5%
196 normal donkey serum. Primary antibodies utilized were goat anti-Olig2 (1:100, R&D Systems),
197 mouse anti-CC1 (1:50, Millipore), mouse IgG2a anti-SOX2 (1:100, R&D Systems), mouse IgG1
198 anti-Ki67 (1:25, Fisher Scientific), rat IgG2a anti-MBP (1:300, Abcam Inc.), goat IgG Smi311 &
199 Smi312 (1:1000, BioLegend), rabbit IgG anti-App (1:500, Thermo Fisher), rabbit IgG anti-Iba1
200 (1:300, Wako Chemicals), and mouse IgG1 anti-Gfap (1:400, Sigma-Aldrich). Alexa 488, 594,
201 and 647-conjugated secondary antibodies (Invitrogen) were used at 1:500. Lesion areas were
202 captured at 10X and 20X magnification using an Olympus IX83 with IX3-SSU motorized stage
203 and image tiles stitched via cellSens software. Images of immunostained sections were aligned
204 with their corresponding FloroMyelin stained section to accurately mark lesion boundaries, with
205 exclusion of any portion of the lesion which extends into the gray matter. Cells counts were
206 determined via a deep learning (machine learning) augmented process (code available upon
207 request), validated with multi-counter manual counts. The Keras based convolution network was
208 trained on a set of ~3250 CC1 positive and ~3250 CC1 negative pre-classified images
209 (supervised learning).

210 *Statistics*

211 All statistical testing was completed using GraphPad Prism Version 8.4.0 (455). The
212 control group for all analyses of cell number and phenotype was NAWM. Groups comprised either
213 time-points following injection of lysolecithin and/or regional analysis within the lesion. For all
214 reporting, an experimental unit comprised a single lesion. Given the novelty of the method, sample
215 size was based on previous experience with gliotoxin lesions established in mouse and rat. A
216 minimum of 4 experimental units (lesions) per group was set *a priori* and along with a requirement
217 for at least three animals per group. Criteria for lesion inclusion were established *a priori*. Only
218 lesions located within internal capsule white matter were included in the analysis. No white matter
219 lesions regardless of size were excluded from the analysis. Rabbits were allocated to each group
220 in a randomized fashion based on availability from the vendor and surgical schedule. Manual cell
221 counting for all quantitative measures was performed in a blinded fashion. Normality of data was
222 tested in GraphPad using the D'Agostino-Pearson omnibus test. For analysis of time-series data,
223 one-way ANOVA with Tukey's post-hoc testing was performed. For analysis of time-series and
224 region delimited data, two-way ANOVA with Sidak's post-hoc testing was performed.

225 *Data availability*

226 The data that support the findings of this study are available upon reasonable request.

227

228 **RESULTS**

229 **Abundant OPC recruitment is universal in rodent models but is relatively uncommon in**
230 **MS lesions.**
231 To compare OPC recruitment between experimental models and human disease, we performed
232 a meta-analysis of absolute and relative OPC densities following demyelination. While the
233 recruitment of OPCs occurs following demyelination in MS, the density of OPCs found within
234 lesions does not exceed that of normal appearing white matter (NAWM) (**Supplemental Figure**
235 **1A**). In contrast, rodent models of toxin-induced demyelination are associated with
236 supernumerary OPC recruitment and highly efficient remyelination [20, 21](**Supplemental Figure**
237 **1B**). Likewise, following inflammatory demyelination or viral-mediated encephalomyelitis with
238 attendant axonal injury and immune cell responses, OPC recruitment is similarly robust
239 (**Supplemental Figure 1C**). As such, we hypothesized that supernumerary densities of OPCs
240 are necessary for efficient remyelination, and that MS lesion tissue displays relatively weak OPC
241 recruitment because OPC recruitment becomes rate-limiting as lesion volume increases.

242 **Lysolecithin-induced lesions in the rabbit were larger and more persistent than those**
243 **created in smaller rodent models.**
244 In order to test the hypothesis that lesion volume influences OPC recruitment we sought an
245 experimental species which had white matter structures that would allow for the production of
246 lesions significantly larger than those induced in mice and rats. We selected the rabbit brain as
247 the accessible white matter volume was 6 to 14 times larger [22] then current rodent models, and
248 we predicted that lesions could be generated with cross-sectional areas between 10 and 40 times
249 greater than rat and mouse brain (**Fig. 1A**, ovals). To induce demyelination, we stereotactically
250 injected lysolecithin into the internal capsules of adult NZW rabbits (bilateral injections of 1%
251 lysolecithin, 5 µl). We first examined lesion formation at 14 days post lesion (dpl). Similar to murine
252 lesions, lysolecithin induced profound focal demyelination at the site of injection and a clearly
253 demarcated region of hypercellularity that precisely matched the region of myelin loss (**Fig. 1B**,
254 white dashed line). Volumetric analysis by serial section reconstruction of the lesion indicated a
255 comet-like appearance with a relatively spherical region of demyelination corresponding to the
256 site of injection and a tapered region extending in the posterior-ventral direction, likely due to
257 diffusion within the fascicles of the internal capsule. The mean cross-sectional area and volume
258 peaked at 14 dpl (area: 2.21 ± 0.3 mm^2, volume: 3.29 ± 0.3 mm^3, n = 8) (**Fig. 1C-D**). Compared
259 to mouse, rabbit lesions were over 8-fold larger in volume and a 20-fold increase in maximal
260 cross-sectional area (**Fig. 1B-C**). Intriguingly, the 8-fold increased volume in rabbit exceeded the

261 5-fold increase in volume of lysolecithin injected. Following the peak in lesion area at 14 dpl, lesion
262 area gradually declined with time (21 vs 14 days, Tukey's p = 0.0280). In stark contrast to both
263 mouse and rat models, large regions of demyelination persisted in the rabbit even at 56 dpl by
264 which time rodent models have typically completed remyelination (**Fig. 1E**).

265 **Rabbit lesions represent areas of demyelination with preserved axons and prolonged**
266 **gliotic response.**

267 Next, we sought to characterize the extent of the gliotic response in these lesions, as well as
268 determine the extent of axonal injury and loss in this new model. MBP staining showed abundant
269 myelin debris at 7 dpl, with substantial clearance by 14 dpl (**Fig. 2A**). At 56 dpl, there was a partial
270 recovery of MBP immunoreactivity, but lacked the structure observed in NAWM (**Fig. 2A**).
271 Consistent with primary demyelination, a large number of neurofilament (NF)-labelled axons
272 persisted following demyelination (7-56 dpl) (**Fig. 2B**). We observed a gradient of axonal density
273 with greater numbers of axons at the lesion edge (**Fig. 2B**) (**Fig. 3**). Interestingly, low axonal
274 densities in the lesion core is similarly observed in MS lesions [23]. Additionally, axonal density did
275 not decrease further beyond 7 dpl, based on a qualitative analysis (**Fig. 3**). Consistent with an
276 initial injury, we observed evidence of axonal dysfunction by accumulation of App
277 immunoreactivity at 7 dpl and a decline in the overall proportion of App^+NF^+ axons thereafter (**Fig.**
278 **2B**). Retraction bulbs, a common feature of MS lesion tissue [17], were noted at all timepoints in
279 and around the lesions (**Fig. 3**).

280 All lesions exhibited increased numbers of astrocytes (Gfap) and microglia/macrophages
281 (Iba1), with the greatest number of microglia localized within the lesion core (**Fig. 2C-D**). Within
282 the core, ameboid microglia commonly formed vesicular structures that were surrounded by $Gfap^+$
283 astrocytic processes (**Supplemental Figure 2**). In addition to astrocytes and microglia, fibroblasts
284 are recruited into mouse spinal cord lysolecithin and EAE lesions [24]. However, we observed few
285 $Col1^+$ (fibroblast) cells within the lesion at 7 dpl and no $Col1^+$ cells at 56 dpl (data not shown).
286 Next, we quantified the overall gliotic (microglial and astrocytic) response by determining the
287 density of nonoligodendrocyte lineage cell population (nonOligo, $Olig2^-DAPI^+$) within the lesion at
288 each time point. The density of nonOligos increased 10-fold following injury, with densities
289 peaking at 14 dpl (NAWM (n = 20) vs 14dpl (n = 7), Tukey's p <0.0001) (**Fig. 2F**). While there
290 was a statistically significant decrease in NonOligo cell density between 14 and 56 dpl (14dpl (n
291 = 7) vs 56dpl (n = 5), Tukey's p < 0.0001), the percentage of nonOligos remained constant (14dpl
292 (n = 7) vs 56dpl (n = 5), Tukey's p = 0.64) (**Fig 2F-G**). However, there was a statistically significant
293 negative trend from 7dpl to 56dpl in the percentage of nonOligos (Test for linear trend, 7dpl to

294 56dpl, slope = -2.7, F (1, 17) = 8.70, p = 0.009). Together, this suggests that the gliotic response
295 is persistent and remains active for at least the first two months following demyelination.

296 **Demyelinated areas show insufficient OPC recruitment and failed to restore normal**
297 **oligodendrocyte cell density.**

298 As recruitment varies greatly between experimental models and MS lesions, we next sought to
299 characterize OPC recruitment and differentiation following demyelination in this new model. We
300 found that total oligodendrocyte lineage (Olig2$^+$) cell density was decreased relative to NAWM at
301 all timepoints and remained so even at 56 dpl (NAWM (n = 22) vs 56dpl (n = 5), Tukey's p =
302 0.003) (**Fig 4A,4E**). There were no statistically significant differences between timepoints in Olig2$^+$
303 cell density (7-56dpl) (One-way ANOVA, F (3, 18) = 0.98, p = 0.42). Importantly, the density of
304 OPCs and immature oligodendrocytes defined as CC1$^-$Olig2$^+$ (**Fig 4D**) was maintained, showing
305 no statistically significant differences between groups (One-way ANOVA, F (4, 28) = 0.88, p =
306 0.49) (**Fig 4F**), a similar observation to that of MS lesion tissue (**Fig 1A**). However, the proportion
307 of OPCs increased significantly at 7dpl (7 dpl (n = 4) vs NAWM (n = 16), Tukey's p <0.0001), but
308 returned to that of NAWM by 56 dpl (n = 5; Tukey's p =0.79) (**Fig 4G**). Sox2 expression is
309 upregulated by Olig2-defined OPCs following demyelination and corresponds with OPC
310 activation, acting to maintain these cells in a proliferative state and priming them for differentiation
311 [4]. In rodents, OPC activation peaked at 5 dpl [4]. Comparatively, Sox2$^+$Olig2$^+$ activated OPCs in
312 the rabbit peaked at 14 dpl (Tukey's multiple comparisons test, NAWM (n = 19) vs 14dpl (n = 4),
313 p = <0.0001), but this peak did not correspond with an increase in total OPC density at 14, 21 or
314 56 dpl (**Fig 4B-4C**). Likewise, the density of Ki67$^+$ proliferating Olig2$^+$ OPCs peaked at 14 dpl and
315 declined thereafter, returning to NAWM levels by 56 dpl (**Fig 4J-4K**).

316 In rodent models, the loss of Sox2 in OPCs and exit from cell cycle correlates with a
317 recovery of mature OL cell density [4]. We analyzed oligodendrogenesis using CC1$^+$Olig2$^+$ at each
318 time point. Unlike the rodent, the density of mature OLs did not return to NAWM levels. Such that
319 at 56 dpl, the density of post-mitotic OLs remained less than half that of oligodendrocytes in
320 NAWM (Tukey's p = 0.0013). However, we noted a significant increase in OL density between 7
321 and 56 dpl (test for linear trend, 7dpl to 56 dpl, F (1, 13) = 4.8, p = 0.047) (**Fig 4D, 4L**). Intriguingly,
322 while the overall density of mature OLs was dramatically reduced in the rabbit, the percentage of
323 mature OLs returned to that of NAWM by 56 dpl (NAWM (n = 16) vs 56dpl (n = 5), Tukey's p =
324 0.79) (**Fig 4M**). These results indicate that while rabbit OPCs remain capable of
325 activation/proliferation and subsequent oligodendrocyte differentiation, the number of OPC
326 recruited following demyelination is insufficient to restore the density of OLs to NAWM levels.

327 **Compared to rodent models, rabbit lesions exhibited inferior OPC recruitment and delayed**
328 **OL generation.**
329 We directly compared the dynamics of OPC recruitment and differentiation in the rabbit to
330 analogous rodent focal models of gliotoxin-induced demyelination. The rabbit internal capsule
331 (IC) contained higher density of Olig2$^+$ cells compared to mouse spinal cord (SC) (**Fig 5A-B**).
332 Following demyelination, recruitment of Olig2$^+$ cells was far more efficient in mouse SC than that
333 observed in rabbit IC (**Fig 5C-D)**. To quantitatively compare OPC recruitment and differentiation
334 across models, we compared our results to those of previous lysolecithin models of demyelination
335 in the mouse [4, 25, 26] and ethidium bromide in the rat caudal cerebral peduncle (CCP)[4, 9, 27, 28].
336 Following induction of demyelination, both mouse and rat exhibit increased density of Olig2$^+$
337 following recruitment of OPCs at 5 dpl and thereafter (black and brown lines, **Fig 5E**). However,
338 the relative density of Olig2$^+$ oligodendroglia in rabbit does not increase following demyelination
339 and is much reduced compared to mouse and rat (gray line, **Fig 5E-5F**). Similarly, while the
340 density of OPCs in NAWM is greater in the rabbit compared to rat and mouse (**Fig 5G**), the spike
341 in relative OPC density that corresponds with successful recruitment after injury is absent in the
342 rabbit (**Fig 5G-5H**). Both mouse and rat display between two and ten-fold increase overall Olig2
343 and OPC density relative to NAWM. In contrast, the rabbit OPC response is muted and delayed
344 relative to the other species. Intriguingly, rabbit lesions also display slower OPC differentiation
345 (both absolute and relative) compared to mouse and rat (**Fig 5A-5D, 5I-5J**). Thus, abundant OPC
346 recruitment seems to be a characteristic of the remyelination-efficient mouse and rat models,
347 while less-abundant OPC recruitment is a shared characteristic between the rabbit model and
348 observations of MS lesions (**Supplemental Fig 1A vs Fig 5H**).

349 **Regional differences in axonal injury correspond to chronic gliosis and prolonged OPC**
350 **activation.**
351 Unlike rodent models with relatively small cross-sectional area, we observed clearly distinct sub-
352 regions within the rabbit lesion. A common feature of rabbit IC lesions was a central core region
353 that displayed a reduced density of axons relative to the rest of the lesion (**Fig 3**). This appears
354 to replicate a common feature of MS lesions which are often found to possess lower axonal
355 density in a central core region [23]. We defined the remainder of the lesion as lesion periphery (**Fig**
356 **6A-C**). The area of the core region remained stable even at 56 dpl while the area of the lesion
357 periphery significantly reduced with time (**Fig 6G-H**), which could be due to resolution of
358 inflammation, tissue edema, and remyelination.

359 At 14 dpl, the lesion core possessed high numbers of both Iba1$^+$ microglia and Gfap$^+$
360 astrocytes (**Fig 6D-F**). At this point, the astrocytic and microglial responses were qualitatively
361 similar in the lesion core and periphery. In contrast, at 56 dpl, hypertrophic and reactive astrocytes
362 were highly enriched around the lesion core, often forming a distinct border indicative of glial scar
363 formation (**Fig 2C**). The density of microglia/macrophages (Iba1$^+$) was greatest at earlier
364 timepoints and was somewhat reduced in the periphery at later timepoints (**Fig 6D-F, 2D**).
365 Quantification of the density of NonOligo cells reflected these observations indicating that more
366 cell nuclei were present in the core at each stage following demyelination and that cell density
367 gradually decreased following 14 dpl (Two-way ANOVA, location factor, $F(1, 38) = 27.47$, p
368 <0.0001) (**Fig 6I**).
369 We analyzed the relative recruitment and differentiation of OPCs in both lesion core and periphery
370 (**Fig 7**). The overall Olig2$^+$ cell density was significantly greater in the lesion periphery then the
371 core regardless of time (Two-way ANOVA, region main effect: $F(1, 41) = 9.30$, $p = 0.004$) (**Fig**
372 **7E**). This difference was seemingly not due to absolute OPC numbers as there was no statistically
373 significant difference between CC1$^-$ OPC and immature OL density of the core and periphery
374 across time ($F(1, 32) = 3.01$, $p = 0.85$) (**Fig 7F**). Furthermore, the density of Sox2$^+$ activated
375 OPCs (**Fig 7H**) or Ki67$^+$ proliferating OPCs (**Fig 7J**) did not differ significantly between regions.
376 However, the proportion of OPCs among the Olig2 fraction consistently exceeded that of NAWM
377 and was greatest in the lesion core ($F(1, 25) = 8.484$, $p = 0.008$)(**Fig 7G, I, K**). At 56 dpl, Sox2$^+$
378 OPCs remained highly abundant representing over half of all OL lineage cells in the core, while
379 the proportion of activated OPCs in periphery had reduced to NAWM levels ($F(1, 32) = 33.24$, p
380 <0.0001). Likewise, while OPC proliferation peaked at 14 dpl in the lesion periphery and decline
381 thereafter, in the lesion core the rate of OPC proliferation continued to rise until 21 dpl and
382 remained substantially higher than NAWM even at 56 dpl ($F(1, 31) = 9.754$, $p = 0.004$). In
383 contrast, the density of CC1$^+$Olig2$^+$ OL was significantly higher in the lesion periphery across time
384 points ($F(3, 28) = 3.379$, $p = 0.032$) (**Fig 7L**). The proportion of OLs dramatically increased from
385 7 to 21 dpl in both lesion core and periphery but also trended toward an overall increase in the
386 lesion periphery ($p = 0.058$) (**Fig 7M**). Together, these results suggest that the core environment
387 could be driving OPCs to a state of chronic activation and proliferation following demyelination
388 while the lesion periphery supported OL differentiation after an initial period of activation and
389 proliferation.

390 **Decreased OL and preserved OPC density in the NAWM directly adjacent to the lesion.**
391 As the larger rabbit lesion afforded a closer examination of regional differences in OPC response
392 to demyelination, we examined the density and proportion of OL lineage cells in and around the
393 border of demyelination. The lesion border was defined by reduced solochrome staining
394 compared to NAWM (**Fig 8A-B**). A region extending 100 µm outside the lesion border was defined
395 as perilesion, while the analogous region within the lesion was classified as the lesion edge (**Fig**
396 **8C**). While the perilesion region was not hypercellular, with DAPI density not exceeding NAWM
397 at 7 dpl, the lesion edge exhibited clear hypercellularity that was reduced compared to lesion
398 periphery and core (**Fig 8D, 8I**). Furthermore, the perilesion did not exhibit detectable
399 demyelination as we confirmed that both MBP and FluoroMyelin were not reduced in this region
400 (data not shown). The remaining lesion was divided into inner periphery and lesion core as
401 described above. Intriguingly, the different regions exhibited significantly distinct temporal
402 increases in cellular density (p = <0.0001), with the greatest density of cells found in the lesion
403 core at between 14 and 21 dpl (**Fig 8D**). Also corresponding with these demarcations, we
404 observed a distinct pattern of OPC and OL lineage fate between each region (**Fig 8E, 8H**). The
405 density of $CC1^{-}Olig2^{+}$ OPC and immature OL cells returned to normal density by 7 dpl within the
406 lesion but was substantially lower in the perilesion region than the NAWM (**Fig 8J**). This suggests
407 that a depletion of OPCs occurs around the site of the lesion as cells are recruited. The density
408 of activated $Sox2^{+}$ OPCs peaked at 14 dpl across regions and was greatest in the central lesion
409 regions (core and inner periphery) (**Fig 8F, 8K**). While the lesion core possessed the greatest
410 proportion of $Sox2^{+}$ OPCs exceeding 50% of $Olig2^{+}$ cells, up to 25% of OL lineage cells expressed
411 Sox2 in the perilesion region (p = 0.005) (**Fig 8F, Fig 8L**). This suggests that OPCs outside the
412 region of demyelination upregulate Sox2 in response to nearby demyelination. Intriguingly, the
413 perilesion exhibited a substantial loss of $Olig2^{+}CC1^{+}$ OL. In contrast, the perilesion region in
414 mouse spinal cord lesions, which was defined in a similar manner based on the lack of
415 hypercellularity, did not demonstrate OL loss [29]. As expected, OL loss was apparent within the
416 bulk of the rabbit lesion and the relatively small increase in OL density did not differ significantly
417 between regions (p = 0.012) (**Fig 8M-8N**).

418 **DISCUSSION**

419 The inadequacies of current rodent models of demyelination used to study and develop
420 remyelination-inducing therapies could contribute to their lack of successful translation into the
421 clinic. Here, we show that we are able to produce lesions which can more closely approximate
422 the size of lesions and several key pathological features found in MS patients. Among these,
423 rabbit lesions display insufficient oligodendrocyte progenitor cell (OPC) recruitment where OPC
424 density never exceeds that of NAWM. In stark contrast, regardless of the method of demyelination
425 or species used, small rodent models of demyelination universally display OPC densities between
426 two and ten times above that of NAWM shortly following demyelination. Large volume rabbit
427 lesions were more persistent than those produced in small rodents, with areas of demyelination
428 visible for at least two months. This is consistent with previous observations in the rabbit which
429 noted scant remyelination at two weeks post injection of lysolecithin and chronic demyelination
430 persisting for at least six months [30-32]. Additionally, we found region-specific differences in the
431 response of OPCs to demyelination, notably chronic activation of OPCs in the core and relatively
432 higher OL generation in the periphery.

433 In small rodent models, OPC recruitment is not considered rate-limiting for remyelination
434 following lysolecithin-induced demyelination [13, 33]. OL differentiation is dependent on the local
435 density of OPCs both *in vitro* [34] and following transplantation into hypomyelinated *shiverer* mice
436 [35]. This suggests that below a certain threshold local density of OPCs, the process of OL
437 differentiation will be limited. Consist with this hypothesis, remyelinated (RM) lesions and active
438 lesions in MS, which have a higher propensity for remyelination, tend to have higher densities of
439 OPCs then chronic demyelinated lesions [36]. Unlike rodent models, the large volume rabbit lesion
440 is associated with inefficient and slow OPC recruitment. Together with the huge difference in
441 volume between rabbit and mouse, this suggests that recruitment may become rate-limiting with
442 increasing lesion volume and that improving recruitment could be a vital and previously
443 underappreciated step in remyelination therapeutics.

444 While we have observed insufficient OPC recruitment in the setting of larger lesion
445 production, we cannot entirely rule out whether failed OPC recruitment is due to volume or
446 species-dependent differences. There are several well described differences in the behavior of
447 human and mouse OPCs both *in vitro* and following transplantation. For example, adult mouse
448 OPCs are more than twice as migratory compared to adult human OPCs [37]. Developmentally,
449 there are vast differences in the volume and proportion of myelination required in the human
450 compared to rodents, with developmental myelination completing over years in the human but
451 weeks in rodents [35]. These differences are also reflected at a cell autonomous level, as, following

452 transplantation human OPCs take 8-12 weeks to generate myelin-forming OLs [38], while equivalent
453 rodent cells typically complete the process of differentiation in 3-4 weeks [39]. In contrast, the
454 majority of signaling cascades and transcriptional networks appear to be largely conserved
455 between primary human and mouse OPCs [40-43]. Regardless of the contribution of OPC species-
456 differences, the failure of OPC recruitment in the rabbit recapitulates that observed in the majority
457 of MS lesions and thereby provides a suitable test bed for therapeutic approaches to improve the
458 migration and proliferation of OPCs.

459 Several other causes of remyelination failure have been proposed. Among these, age is
460 a critical factor determining the success for a number of regenerative processes [44]. While young
461 adult animals efficiently remyelinate following focal demyelination and demonstrate widespread
462 OPC recruitment, aged adult animals display substantially impaired rate of remyelination [27]. In
463 aged adult rodent, OPC recruitment and differentiation are delayed and intriguingly OPC
464 recruitment exhibits a gradient with greatest density in the lesion periphery vs central core [27].
465 Future studies will need to investigate the role of aging in the rabbit model to address whether
466 aging similarly influences both recruitment and differentiation in large volume lesions. In addition
467 to age, the innate immune response and extent of axonal injury are critical components that
468 determining the success or failure or remyelination.

469 Axonal degeneration and transection in MS occurs in the context of inflammatory
470 processes associated with (1) primary demyelination, (2) following the loss of trophic support by
471 myelinating OL and, in some cases, (3) independently of overt demyelination [45]. While loss of
472 trophic support by myelinating OLs results in axonal injury [46], it is likely that axonal damage in
473 active lesions is due to the intense proinflammatory and toxic microenvironment [17, 47]. Interestingly
474 in experimental models, axonal damage peaks at 6 days following induction of demyelination and
475 decreases substantially thereafter, corresponding to the differentiation of OPCs into myelinating
476 OLs [48]. Further supporting the association of axonal injury and myelin regeneration, induction of
477 OL differentiation and remyelination following ablation of the muscarinic receptor in OPCs
478 prevents axonal loss in EAE [49]. In contrast, an increase in pro-inflammatory signaling such as
479 IFN-γ administered at the time of demyelination prevents efficient OPC recruitment and
480 exacerbates axonal injury [50]. Likewise, in the rabbit model we observed axonal loss and injury
481 marked by App1 following demyelination at 7 dpl. Axonal loss was greatest in the lesion core and
482 the distribution of axonal loss in rabbit lesions was similar to that observed in MS [23]. Axonal loss
483 in the rabbit was largely associated with the initial gliotoxin insult as the size of core region
484 remained stable out to 56 dpl and we noted a substantial reduction in App1 staining after 7 dpl.
485 Interestingly, the microenvironment of the core region likely influences OPC state. Within the core

486 we observed many more OPCs that remained activated and proliferative for at least two months
487 following demyelination. Prolonged activation of OPCs within the core correlated with increased
488 microglial density suggesting that regional differences in microglial signaling alter OPC state.

489 Recent studies have increasingly highlighted the role that the innate immune response
490 plays in influencing remyelination [51]. OPC recruitment and differentiation is dependent on the
491 polarization of microglia/macrophages, whereby a proinflammatory so-called M1 state promotes
492 OPC recruitment while an immunoregulatory M2 state promotes OPC differentiation and
493 remyelination [52]. The transition of microglia/macrophages to M2 polarization can be blocked by
494 preventing necroptosis of M1 microglia and blocking this transition impairs remyelination of
495 demyelinated cerebellar explants [53]. While type 1 interferon may recruit microglia into regions of
496 demyelination, type 2 interferon (IFN-γ) produced by Th1 cells is associated with and found at
497 high levels during active lesion formation in MS [54]. Interestingly, IFN-γ directly drives OPC
498 quiescence via upregulation of PRRX1 in human OPCs [55]. This can be reversed by modulation
499 of pharmacological modulation of the local heparanome within regions of demyelination rescuing
500 both remyelination and axonal injury [50]. It is interesting to speculate that in large volume lesions,
501 the transition of the microglia/macrophage response from proinflammatory to immunomodulatory
502 phenotype occurs before the lesion achieves a sufficient density of OPC and thereby instead of
503 promoting remyelination acts instead to limit OPC recruitment resulting in an overall failure of
504 myelin regeneration. Whether or not this occurs in the complex inflammatory milieu of MS lesions
505 will need to be determined.

506 Remyelination in gliotoxin models provides a simplified model to study the cellular
507 mechanisms of myelin regeneration. While several molecular mechanisms have been described
508 that regulate and are rate-limiting for the repair of mouse and rat lesions, similar studies have not
509 yet been performed in large volume lesions. In the present study, we have shown that aberrations
510 in OPC recruitment and differentiation, akin to those observed in MS, occur following the induction
511 of white matter lesions in the rabbit. These lesions were over 20-fold larger than those produced
512 in mice and exhibit axon injury/loss as well as prolong gliosis that correspond with similar active
513 lesions in MS lesions. OPC recruitment is profoundly different in the rabbit model compared to
514 small rodents as the density of OPCs never exceeds that of NAWM. This corresponds well with
515 observations of OPC density in human MS lesions. Unlike other large species (cat, dog, sheep or
516 pig) with larger volumes of available white matter, rabbits are cost-effective and stereotaxic
517 techniques are routinely accessible in most neuroscience laboratories. As such, we propose that
518 the simplicity and accessibly of the rabbit model along with the clear differences in lesion
519 environment and patterns of OPC recruitment and differentiation will provide a vital

520 complementary approach for preclinical testing of remyelination therapeutics and aid in the
521 successful development of clinical interventions aimed at promoting myelin regeneration.

522 **REFERENCES**

523 1. Confavreux C, Vukusic S, Moreau T, Adeleine P. Relapses and progression of disability
524 in multiple sclerosis. *The New England journal of medicine*. Nov 16 2000;343(20):1430-8.
525 doi:10.1056/NEJM200011163432001
526 2. Franklin RJM, Ffrench-Constant C. Regenerating CNS myelin - from mechanisms to
527 experimental medicines. *Nat Rev Neurosci*. Nov 16 2017;18(12):753-769.
528 doi:10.1038/nrn.2017.136
529 3. Hughes EG, Kang SH, Fukaya M, Bergles DE. Oligodendrocyte progenitors balance
530 growth with self-repulsion to achieve homeostasis in the adult brain. *Nature neuroscience*. Jun
531 2013;16(6):668-76. doi:10.1038/nn.3390
532 4. Zhao C, Ma D, Zawadzka M, et al. Sox2 Sustains Recruitment of Oligodendrocyte
533 Progenitor Cells following CNS Demyelination and Primes Them for Differentiation during
534 Remyelination. *J Neurosci*. Aug 19 2015;35(33):11482-99. doi:10.1523/JNEUROSCI.3655-
535 14.2015
536 5. Lubetzki C, Sol-Foulon N, Desmazieres A. Nodes of Ranvier during development and
537 repair in the CNS. *Nat Rev Neurol*. Aug 2020;16(8):426-439. doi:10.1038/s41582-020-0375-x
538 6. Wolswijk G. Chronic stage multiple sclerosis lesions contain a relatively quiescent
539 population of oligodendrocyte precursor cells. *J Neurosci*. Jan 15 1998;18(2):601-9.
540 7. Mi S, Miller RH, Lee X, et al. LINGO-1 negatively regulates myelination by
541 oligodendrocytes. *Nature neuroscience*. Jun 2005;8(6):745-51. doi:10.1038/nn1460
542 8. Zhang M, Zhan XL, Ma ZY, Chen XS, Cai QY, Yao ZX. Thyroid hormone alleviates
543 demyelination induced by cuprizone through its role in remyelination during the remission period.
544 *Exp Biol Med (Maywood)*. Sep 2015;240(9):1183-96. doi:10.1177/1535370214565975
545 9. Neumann B, Baror R, Zhao C, et al. Metformin Restores CNS Remyelination Capacity by
546 Rejuvenating Aged Stem Cells. *Cell Stem Cell*. Oct 3 2019;25(4):473-485 e8.
547 doi:10.1016/j.stem.2019.08.015
548 10. Green AJ, Gelfand JM, Cree BA, et al. Clemastine fumarate as a remyelinating therapy
549 for multiple sclerosis (ReBUILD): a randomised, controlled, double-blind, crossover trial. *Lancet*.
550 Dec 2 2017;390(10111):2481-2489. doi:10.1016/S0140-6736(17)32346-2
551 11. Mellion M, Edwards KR, Hupperts R, et al. Efficacy Results from the Phase 2b SYNERGY
552 Study: Treatment of Disabling Multiple Sclerosis with the Anti-LINGO-1 Monoclonal Antibody
553 Opicinumab. *Neurology*. Apr 18 2017;88

554 12. Klistorner A, Chai Y, Leocani L, et al. Assessment of Opicinumab in Acute Optic Neuritis
555 Using Multifocal Visual Evoked Potential. *CNS Drugs*. Dec 2018;32(12):1159-1171.
556 doi:10.1007/s40263-018-0575-8
557 13. Woodruff RH, Fruttiger M, Richardson WD, Franklin RJ. Platelet-derived growth factor
558 regulates oligodendrocyte progenitor numbers in adult CNS and their response following CNS
559 demyelination. *Mol Cell Neurosci*. Feb 2004;25(2):252-62. doi:10.1016/j.mcn.2003.10.014
560 14. Foerster S, Neumann B, McClain C, et al. 2020;doi:10.1101/2020.05.21.108373
561 15. Xing YL, Chuang BHA, Poh J, et al. 2021;doi:10.1101/2021.05.13.443012
562 16. Mason JL, Toews A, Hostettler JD, et al. Oligodendrocytes and progenitors become
563 progressively depleted within chronically demyelinated lesions. *The American journal of*
564 *pathology*. May 2004;164(5):1673-82. doi:10.1016/S0002-9440(10)63726-1
565 17. Trapp BD, Peterson J, Ransohoff RM, Rudick R, Mork S, Bo L. Axonal transection in the
566 lesions of multiple sclerosis. *The New England journal of medicine*. Jan 29 1998;338(5):278-85.
567 doi:10.1056/NEJM199801293380502
568 18. Jean I, Lavialle C, Barthelaix-Pouplard A, Fressinaud C. Neurotrophin-3 specifically
569 increases mature oligodendrocyte population and enhances remyelination after chemical
570 demyelination of adult rat CNS. *Brain Res*. May 16 2003;972(1-2):110-8.
571 19. Rusielewicz T, Nam J, Damanakis E, John GR, Raine CS, Melendez-Vasquez CV.
572 Accelerated repair of demyelinated CNS lesions in the absence of non-muscle myosin IIB. *Glia*.
573 Apr 2014;62(4):580-91. doi:10.1002/glia.22627
574 20. Shields SA, Gilson JM, Blakemore WF, Franklin RJ. Remyelination occurs as extensively
575 but more slowly in old rats compared to young rats following gliotoxin-induced CNS demyelination.
576 *Glia*. Oct 1999;28(1):77-83.
577 21. Arnett HA, Fancy SP, Alberta JA, et al. bHLH transcription factor Olig1 is required to repair
578 demyelinated lesions in the CNS. *Science*. Dec 17 2004;306(5704):2111-5.
579 doi:10.1126/science.1103709
580 22. Zhang K, Sejnowski TJ. A universal scaling law between gray matter and white matter of
581 cerebral cortex. *Proc Natl Acad Sci U S A*. May 9 2000;97(10):5621-6.
582 doi:10.1073/pnas.090504197
583 23. Ferguson B, Matyszak MK, Esiri MM, Perry VH. Axonal damage in acute multiple sclerosis
584 lesions. *Brain*. Mar 1997;120 (Pt 3):393-9. doi:10.1093/brain/120.3.393
585 24. Dorrier CE, Aran D, Haenelt EA, et al. CNS fibroblasts form a fibrotic scar in response to
586 immune cell infiltration. *Nature neuroscience*. Feb 2021;24(2):234-244. doi:10.1038/s41593-020-
587 00770-9

588 25. Kucharova K, Stallcup WB. NG2-proteoglycan-dependent contributions of
589 oligodendrocyte progenitors and myeloid cells to myelin damage and repair. *J Neuroinflammation*.
590 Sep 4 2015;12:161. doi:10.1186/s12974-015-0385-6
591 26. Fancy SP, Baranzini SE, Zhao C, et al. Dysregulation of the Wnt pathway inhibits timely
592 myelination and remyelination in the mammalian CNS. *Genes Dev*. Jul 1 2009;23(13):1571-85.
593 doi:10.1101/gad.1806309
594 27. Sim FJ, Zhao C, Penderis J, Franklin RJ. The age-related decrease in CNS remyelination
595 efficiency is attributable to an impairment of both oligodendrocyte progenitor recruitment and
596 differentiation. *J Neurosci*. Apr 1 2002;22(7):2451-9. doi:20026217
597 28. Syed YA, Hand E, Mobius W, et al. Inhibition of CNS remyelination by the presence of
598 semaphorin 3A. *J Neurosci*. Mar 9 2011;31(10):3719-28. doi:10.1523/JNEUROSCI.4930-10.2011
599 29. Crawford AH, Tripathi RB, Foerster S, et al. Pre-Existing Mature Oligodendrocytes Do Not
600 Contribute to Remyelination following Toxin-Induced Spinal Cord Demyelination. *Am J Pathol*.
601 Mar 2016;186(3):511-6. doi:10.1016/j.ajpath.2015.11.005
602 30. Blakemore WF. Observations on remyelination in the rabbit spinal cord following
603 demyelination induced by lysolecithin. *Neuropathology and applied neurobiology*. Jan-Feb
604 1978;4(1):47-59. doi:10.1111/j.1365-2990.1978.tb00528.x
605 31. Waxman SG, Kocsis JD, Nitta KC. Lysophosphatidyl choline-induced focal demyelination
606 in the rabbit corpus callosum. Light-microscopic observations. *J Neurol Sci*. Dec 1979;44(1)(45-
607 53):45-53. doi:10.1016/0022-510x(79)90221-1
608 32. Foster RE, Kocsis JD, Malenka RC, Waxman SG. Lysophosphatidyl choline-induced focal
609 demyelination in the rabbit corpus callosum. Electron-microscopic observations. *J Neurol Sci*. Nov
610 1980;48(2):221-31. doi:10.1016/0022-510x(80)90202-6
611 33. Woodruff RH, Franklin RJ. Demyelination and remyelination of the caudal cerebellar
612 peduncle of adult rats following stereotaxic injections of lysolecithin, ethidium bromide, and
613 complement/anti-galactocerebroside: a comparative study. *Glia*. Feb 1 1999;25(3):216-28.
614 doi:10.1002/(SICI)1098-1136(19990201)25:3<216::AID-GLIA2>3.0.CO;2-L [pii]
615 34. Rosenberg SS, Kelland EE, Tokar E, De la Torre AR, Chan JR. The geometric and spatial
616 constraints of the microenvironment induce oligodendrocyte differentiation. *Proc Natl Acad Sci U*
617 *S A*. Sep 23 2008;105(38):14662-7. doi:10.1073/pnas.0805640105
618 35. Dietz KC, Polanco JJ, Pol SU, Sim FJ. Targeting human oligodendrocyte progenitors for
619 myelin repair. *Exp Neurol*. Sep 2016;283(Pt B):489-500. doi:10.1016/j.expneurol.2016.03.017

620 36. Boyd A, Zhang H, Williams A. Insufficient OPC migration into demyelinated lesions is a
621 cause of poor remyelination in MS and mouse models. *Acta Neuropathol*. Jun 2013;125(6):841-
622 59. doi:10.1007/s00401-013-1112-y
623 37. Bribian A, Medina-Rodriguez EM, Josa-Prado F, et al. Functional Heterogeneity of Mouse
624 and Human Brain OPCs: Relevance for Preclinical Studies in Multiple Sclerosis. *J Clin Med*. Jun
625 2 2020;9(6)doi:10.3390/jcm9061681
626 38. Sim FJ, McClain CR, Schanz SJ, Protack TL, Windrem MS, Goldman SA. CD140a
627 identifies a population of highly myelinogenic, migration-competent and efficiently engrafting
628 human oligodendrocyte progenitor cells. *Nat Biotechnol*. Sep 25 2011;29(10):934-41.
629 doi:10.1038/nbt.1972
630 39. Baron-Van Evercooren A, Blakemore WF. Chapter 6 - Remyelination through
631 Engraftment. In: Lazzarini RA, Griffin JW, Lassman H, Nave K-A, Miller R, Trapp BD, eds. *Myelin*
632 *Biology and Disorders*. Academic Press; 2004:143-172.
633 40. Conway GD, O'Bara MA, Vedia BH, Pol SU, Sim FJ. Histone deacetylase activity is
634 required for human oligodendrocyte progenitor differentiation. *Glia*. Dec 2012;60(12):1944-53.
635 doi:10.1002/glia.22410
636 41. Abiraman K, Pol SU, O'Bara MA, et al. Anti-muscarinic adjunct therapy accelerates
637 functional human oligodendrocyte repair. *J Neurosci*. Feb 25 2015;35(8):3676-88.
638 doi:10.1523/JNEUROSCI.3510-14.2015
639 42. Pol SU, Polanco JJ, Seidman RA, et al. Network-Based Genomic Analysis of Human
640 Oligodendrocyte Progenitor Differentiation. *Stem Cell Reports*. Aug 8 2017;9(2):710-723.
641 doi:10.1016/j.stemcr.2017.07.007
642 43. Saraswat D, Shayya HJ, Polanco JJ, et al. Overcoming the inhibitory microenvironment
643 surrounding oligodendrocyte progenitor cells following experimental demyelination. *Nat Commun*.
644 Mar 26 2021;12(1):1923. doi:10.1038/s41467-021-22263-4
645 44. Ruckh JM, Zhao JW, Shadrach JL, et al. Rejuvenation of regeneration in the aging central
646 nervous system. *Cell Stem Cell*. Jan 6 2012;10(1):96-103. doi:10.1016/j.stem.2011.11.019
647 45. Haines JD, Inglese M, Casaccia P. Axonal damage in multiple sclerosis. *Mt Sinai J Med*.
648 Mar-Apr 2011;78(2):231-43. doi:10.1002/msj.20246
649 46. Nave KA. Myelination and the trophic support of long axons. *Nature reviews*
650 *Neuroscience*. Apr 2010;11(4):275-83. doi:10.1038/nrn2797
651 47. Kornek B, Storch MK, Weissert R, et al. Multiple sclerosis and chronic autoimmune
652 encephalomyelitis: a comparative quantitative study of axonal injury in active, inactive, and

653 remyelinated lesions. *The American journal of pathology*. Jul 2000;157(1):267-76.
654 doi:10.1016/S0002-9440(10)64537-3
655 48. Schultz V, van der Meer F, Wrzos C, et al. Acutely damaged axons are remyelinated in
656 multiple sclerosis and experimental models of demyelination. *Glia*. Aug 2017;65(8):1350-1360.
657 doi:10.1002/glia.23167
658 49. Mei F, Lehmann-Horn K, Shen YA, et al. Accelerated remyelination during inflammatory
659 demyelination prevents axonal loss and improves functional recovery. *Elife*. Sep 27
660 2016;5:e18246. doi:10.7554/eLife.18246
661 50. Saraswat D, Welliver RR, Ravichandar R, et al. Heparanome-Mediated Rescue of
662 Oligodendrocyte Progenitor Quiescence following Inflammatory Demyelination. *J Neurosci*. Mar
663 10 2021;41(10):2245-2263. doi:10.1523/JNEUROSCI.0580-20.2021
664 51. Lloyd AF, Miron VE. The pro-remyelination properties of microglia in the central nervous
665 system. Review. *Nat Rev Neurol*. Aug 2019;15(8):447-458. doi:10.1038/s41582-019-0184-2
666 52. Miron VE, Boyd A, Zhao JW, et al. M2 microglia and macrophages drive oligodendrocyte
667 differentiation during CNS remyelination. *Nat Neurosci*. Sep 2013;16(9):1211-8.
668 doi:10.1038/nn.3469
669 53. Lloyd AF, Davies CL, Holloway RK, et al. Central nervous system regeneration is driven
670 by microglia necroptosis and repopulation. *Nat Neurosci*. Jul 2019;22(7):1046-1052.
671 doi:10.1038/s41593-019-0418-z
672 54. Panitch HS. Interferons in Multiple Sclerosis. *Drugs*. 1992/12/01 1992;44(6):946-962.
673 doi:10.2165/00003495-199244060-00004
674 55. Wang J, Saraswat D, Sinha AK, et al. Paired Related Homeobox Protein 1 Regulates
675 Quiescence in Human Oligodendrocyte Progenitors. *Cell reports*. Dec 18 2018;25(12):3435-3450
676 e6. doi:10.1016/j.celrep.2018.11.068
677 56. Rosen GD, Harry JD. Brain volume estimation from serial section measurements: a
678 comparison of methodologies. *J Neurosci Methods*. Nov 1990;35(2):115-24. doi:10.1016/0165-
679 0270(90)90101-k
680 57. Swanson LW. Brain maps 4.0-Structure of the rat brain: An open access atlas with global
681 nervous system nomenclature ontology and flatmaps. *J Comp Neurol*. Apr 15 2018;526(6):935-
682 943. doi:10.1002/cne.24381
683 58. Kuhlmann T, Miron V, Cui Q, Wegner C, Antel J, Bruck W. Differentiation block of
684 oligodendroglial progenitor cells as a cause for remyelination failure in chronic multiple sclerosis.
685 *Brain*. Jul 2008;131(Pt 7):1749-58. doi:10.1093/brain/awn096

686 59. Chang A, Nishiyama A, Peterson J, Prineas J, Trapp BD. NG2-positive oligodendrocyte
687 progenitor cells in adult human brain and multiple sclerosis lesions. *J Neurosci*. Sep 1
688 2000;20(17):6404-12. doi:10.1523/jneurosci.20-17-06404.2000
689 60. Yu Q, Hui R, Park J, et al. Strain differences in cuprizone induced demyelination. *Cell*
690 *Biosci*. 2017;7:59. doi:10.1186/s13578-017-0181-3
691 61. Lin W, Kemper A, Dupree JL, Harding HP, Ron D, Popko B. Interferon-gamma inhibits
692 central nervous system remyelination through a process modulated by endoplasmic reticulum
693 stress. *Brain*. May 2006;129(Pt 5):1306-18. doi:10.1093/brain/awl044
694 62. Zhang J, Zhang ZG, Li Y, et al. Fingolimod treatment promotes proliferation and
695 differentiation of oligodendrocyte progenitor cells in mice with experimental autoimmune
696 encephalomyelitis. *Neurobiol Dis*. Apr 2015;76:57-66. doi:10.1016/j.nbd.2015.01.006
697 63. Garay L, Tungler V, Deniselle MC, Lima A, Roig P, De Nicola AF. Progesterone attenuates
698 demyelination and microglial reaction in the lysolecithin-injured spinal cord. *Neuroscience*. Sep
699 29 2011;192:588-97. doi:10.1016/j.neuroscience.2011.06.065
700 64. Ulrich R, Seeliger F, Kreutzer M, Germann PG, Baumgartner W. Limited remyelination in
701 Theiler's murine encephalomyelitis due to insufficient oligodendroglial differentiation of nerve/glial
702 antigen 2 (NG2)-positive putative oligodendroglial progenitor cells. *Neuropathol Appl Neurobiol*.
703 Dec 2008;34(6):603-20. doi:10.1111/j.1365-2990.2008.00956.x

704

705 **FIGURE LEGENDS**

706 **Figure 1. Large regions of demyelination following injection of lysolecithin into rabbit**
707 **subcortical white matter.** (**A**) Diagram representing injection sites, and white matter tract size
708 for comparison with rat and mouse, drawn to scale (5 mm) (mouse, overlay of lab section; rat
709 overlay of rat brain atlas [57]). (**B**) Lysolecithin-induced lesion in the rabbit stained for FloroMyelin
710 (FM, red) and 4',6'-diamidino-2-phenylindole (DAPI, blue). White dotted line indicates lesion
711 border. (**C-D**) Maximal cross-sectional area (**C**) and lesion volume (**D**) of rabbit lesions at 14 dpl
712 (peak lesion volume, *n* = 8), compared to that seen in lysolecithin mouse models [18, 19]. (**E**) Maximal
713 cross-sectional area of lesions following lysolecithin injection in rabbit (*n* = 6-8) and rat [33] (dpl,
714 days post-lesion). Mean ± SEM shown. Scale: 500 µm.

715

716 **Figure 2. Evolution of rabbit demyelinating lesions with preserved axon integrity and**
717 **prolonged gliotic response.** (**A-D**) Representative confocal images of normal appearing white
718 matter (NAWM) stained for myelin, axonal, astrocytic and microglial/macrophage markers.
719 Following demyelination at 7 to 56 days post lesion (dpl), lesions were imaged by widefield
720 epifluorescence (outlined with dotted white line) shown in the left panel. Higher power confocal
721 images of the area outlined with the white box are shown in the right panel. (**A**) At 7 dpl, myelin
722 basic protein (Mbp, gray) staining demonstrated myelin loss and degeneration within the lesion,
723 and Mbp levels remain depressed over time. (**B**) Axons, stained with neurofilament (NF, green),
724 persist within the lesion bounds even at 56 dpl. Axonal injury (APP, red) is evident at 7dpl but is
725 reduced thereafter following demyelination. (**C-D**) Robust neuroinflammatory response,
726 astrocytes were stained with glial fibrillary acidic protein (Gfap, green) and amyloid microglial cells
727 were stained with ionized calcium binding adaptor molecule 1 (IBA1, red). (**E**) Total DAPI cell
728 density within the lesion was quantified (*n* = 4-19 per group, mean ± SEM). (**F-G**) The non-
729 oligodendrocyte lineage cells (nonOligos) was defined as $DAPI^{+}Olig2^{-}$ cells. Density (**F**) and
730 proportion of total cells (**G**) was quantified (*n* = 4-19). The density of cells increases dramatically
731 following lysolecithin injection and peaks at 14 days. This is largely due to an increase in the
732 density of non-oligodendrocyte lineage cells which likely represents microglia and at later time-
733 points astrocytic influx and proliferation (**G**). Lesion image scale: 500 µm. Confocal scale: 25 µm.

734

735 **Figure 3 (related to Figure 3). Lesions were composed of an axon deficient core, with**
736 **higher axon preservation in the periphery.** Representative 60x oil immersion objective +
737 constrained iterative deconvolution stitched images (0.8 µm steps over 4µm depth) of NAWM (**A**)
738 or following lysolecithin injection (**B-E**) stained for neurofilament (NF, green) and/or DAPI (blue).

739 White dotted lines indicate lesion borders and green dotted lines represents lesion cores.
740 Retraction bulbs were observed in and around the lesions at all timepoints (small frame images
741 found in **B-E**). Scale bar: 100um.
742
743 **Figure 4. Insufficient OPC recruitment and oligodendrocyte generation following**
744 **demyelination in rabbit white matter.** (**A**) Olig2 (red) was used to identify total oligodendrocyte
745 lineage cell density (NAWM, 14dpl, and 56 dpl shown). Insert shows high magnification of labelled
746 cells. Activated $Sox2^+$ OPCs (**B**, cyan), proliferative $Ki67^+$ OPCs (**C**, gray) and mature $CC1^+$
747 oligodendrocyte (**D**, green) were identified by colocalization with Olig2. Additionally, Sox2 has
748 been noted to be expressed by a subpopulation of astrocytes [4], which are identified as $Sox2^+Olig2^-$
749 cells. (**E**) Oligodendrocyte lineage cell density was significantly depressed relative to NAWM
750 following demyelination (*n* = 4-22, one-way ANOVA). The density and proportion of OPCs defined
751 as either $Olig2^+CC1^-$ (**F-G**), $Sox2^+Olig2^+$ (**H-I**) or $Ki67^+Olig2^+$ (**J-K**) increased following
752 demyelination and peaked between 7-14 dpl. While the proportion of mature oligodendrocytes
753 ($Olig2^+CC1^+$) (**M**) increased following demyelination, the overall density remained significantly
754 depressed relative to NAWM (**L**). Mean ± SEM. Tukey's multiple comparisons post-test vs.
755 NAWM. **, ***, and **** indicate $p < 0.01$, 0.001, and 0.0001, respectively. Large frame scale: 50
756 µm. Small frame scale; 20 µm.
757
758 **Figure 5. Rabbit lesions show delayed recruitment of OPCs, abundant Sox2 activation, and**
759 **slower maturation of oligodendrocytes compared to rodent models.** Representative images
760 of normal appearing white matter (NAWM) of mouse spinal cord (**A**) and rabbit internal capsule
761 (**B**). Mature oligodendrocytes and OPCs identified as $Olig2^+CC1^+$ and $Olig2^+CC1^-$, respectively.
762 Comparative images of lysolecithin induced lesions in mouse (**C**) and rabbit (**D**) at 14 dpl. White
763 dashed line indicates lesion border. *L* indicates lesion area when border is visible. (**E-J**)
764 Comparison of oligodendrocyte lineage cell response following demyelinating lesions between
765 rabbit (gray), mouse (black), and rat (brown). Density and relative change in density compared to
766 NAWM of that species. (**E-F**) While $Olig2^+$ cell density increases relative to NAWM following lesion
767 production in mouse [4] and rats [4], it remains depressed in rabbits. (**G-H**) Relative to NAWM, OPC
768 density in rat [27] (Pdgfra $mRNA^+$) and mouse [25] ($NG2^+$) models increases greatly following lesion
769 production. Conversely, OPC density in the rabbit ($CC1^-Olig2^+$) does not significantly change from
770 NAWM. (**I-J**) Mature OLs determined by $Olig2^+PLP^+$ (mouse [26], black), or $Olig2^+CC1^+$ (rat [9, 28],
771 rabbit). Rat mature OL density curve was determined from two separate studies, with NAWM
772 (original data: 326.4 ± 27.1 cells/mm^2) and 10dpl (original data: 102.2 ± 14.7 cells/mm^2) data from

773 Syed et al. 2011 normalized to the results of Neumann et al. 2019 (7, 21, 49 dpl). Mean ± SEM
774 shown. Scale bar: 100 μm.
775
776 **Figure 6. Axonal deficient lesion core does not expand with time following demyelination.**
777 Representative images following demyelination at 14 days post lesion (dpl), stained for axons
778 with neurofilament (NF, green), axonal injury with beta amyloid precursor protein (App, Red), and
779 nuclei with DAPI (blue)(**A**) or astrocytes (Gfap, green), and Iba1$^+$ microglia/macrophages (red)(**D**).
780 Lesion border was defined by hypercellularity and FluoroMyelin staining (blue dashed line) and
781 core was defined as a region containing sparse NF$^+$ intact axons (green dashed line). (**B-C, E-F**)
782 High power confocal images of the area outlined with the white boxes in **A** and **D**. (**G-H**) Core
783 lesion area did not significantly change through 56 dpl, while peripheral lesion area decreased
784 with time (*n* = 5-8 per group, two-way ANOVA). (**I**) Quantification of non-oligodendrocyte lineage
785 cells (DAPI$^+$Olig2$^-$ cells). Two-way ANOVA across time points comparing core and periphery
786 indicated a significant difference in the NonOligo cells between core and periphery ($p < 0.0001$),
787 and over time ($p < 0.0001$). The gliotic response was significantly greater in the core compared
788 to the periphery. Sidak's multiple comparisons comparing means of periphery and core at each
789 timepoint. *, **, ***, and **** indicate $p < 0.05$, 0.01, 0.001, and 0.0001, respectively. Mean ± SEM
790 shown. Lesion scale bar: 250 μm. Confocal scale bar: 25 μm.
791
792 **Figure 7. OPCs in the axon-sparse core remained activated and proliferative.** (**A-D**)
793 Representative images following demyelination at 14 days post lesion (dpl), stained for axons
794 with neurofilament (NF, green), activated Olig2$^+$Sox2$^+$ OPCs (**B**, cyan), proliferative Olig2$^+$Ki67$^+$
795 OPCs (**C**, gray) and mature Olig2$^+$CC1$^+$ oligodendrocytes (OL) (**D**, green). (**E**) Quantification of
796 Olig2$^+$ cell density in the core and periphery. Quantification of cell density and proportion of total
797 oligodendrocyte linage cells for OPCs (**F-G**), activated OPCs (**H-I**), proliferative OPCs (**J-K**), and
798 mature OLs (**L-M**). Dotted lines represent cellular density of NAWM. While few intact axons
799 remained, this did not significantly affect the recruitment of OPCs to the lesion core. However, a
800 significantly greater proportion of OPCs were activated and proliferating in the lesion core
801 compared to the periphery. Two-way ANOVA was performed across all time points (TME: time
802 main effect) and comparing core and periphery regions (RME: regional main effect). Sidak's post-
803 test comparing regions at each time point. *, **, ***, and **** indicate $p < 0.05$, 0.01, 0.001, and
804 0.0001, respectively (NAWM: *n* = 19-22, lesion: *n* = 4-7). Mean ± SEM reported. Scale bar: 200
805 μm.
806

807 **Figure 8. Decreased density of mature OLs and no change in OPC density in NAWM directly**
808 **adjacent to demyelinating lesion.** Representative images of NAWM (**A**) and lysolecithin
809 induced lesion at 56 dpl (**B-C**) in the rabbit stained with solochrome cyanine (myelin, black). Blue
810 dashed line indicates lesion border. PeriLesion region (purple) was defined as an area extending
811 ~100 µm past the lesion border. Lesion edge (blue) was defined as an area ~100 µm smaller than
812 the lesion border. Inner periphery (red) was defined as the area between the outer periphery and
813 the core. Core defined as a central area of the lesion where few intact axons were observed.
814 Scale bar: 200 µm. Lesion cross-sectional columns covering the various regions stained for (**D**)
815 DAPI, (**E**) Olig2, (**F**) activated OPCs ($Olig2^+Sox2^+$), (**G**) proliferative OPCs ($Olig2^+Ki67^+$) (**H**) and
816 mature OLs ($Olig2^+CC1^+$). Scale bar, 500 µm. (**I**) Total $DAPI^+$ cell density was quantified in all
817 regions. Quantification of cell density and/or proportion of total oligodendrocyte linage cells
818 between regions for OPCs ($Olig2^+CC1^-$, **J**), Activated OPCs ($Olig2^+Sox2^+$, **K-L**), and mature OLs
819 ($Olig2^+CC1^{+,}$ **M-N**). Dotted lines represent cellular densities of NAWM. Two-way ANOVA was
820 performed across all time points (TME: time main effect) and comparing regions (RME: regional
821 main effect). Mean ± SEM reported (NAWM: *n* = 19-22, lesion: *n* = 4-7).
822
823 **Supplemental Figure 1. OPC density in MS lesions rarely exceeds that of NAWM, but is a**
824 **universal feature of rodent models.** (**A**) In human MS lesions, OPCs were identified as either
825 $Olig2^+Nogo^-$ (green)[36], $Olig2^{strong}$ (blue)[58] or $NG2^+$ cells (orange)[59]. Gray bar indicates the range of
826 observed OPC density from control human white matter (mean ± 1 SD, *n* = 5 patients)[36]. OPC
827 density rarely surpasses that of NAWM. RM = remyelinated lesions. In experimental
828 demyelination, relative OPC density in toxin (**B**) and immune-mediated models (**C**) was plotted
829 against time following the induction of demyelination (lysolecithin and ethidium bromide), or
830 appearance of demyelinated lesions (Cuprizone, EAE, Theiler's virus). OPCs were identified as
831 $NG2^+$ (Cuprizone [60], red; EAE [61, 62], purple; lysolecithin [25, 63], blue; Theiler's virus [64], orange), or
832 Pdgfra $mRNA^+$ (Rat EB [27], green), *n* = 3-5. Horizontal dotted line indicates the normalized OPC
833 density of the mouse. Robust OPC recruitment evidenced by increased OPC density relative to
834 normal white matter was a common feature of all rodent models, regardless of method of
835 demyelination. Rat EB = ethidium bromide induced lesions in the rat. EAE = experimental
836 autoimmune encephalomyelitis. Mean ± SEM shown.
837
838 **Supplemental Figure 2 (related to Figure 3). Amoeboid microglia in lesion core form large**
839 **vesicles surrounded by astrocytic processes.** (**A-B**) Confocal images of NAWM stained for
840 Iba1 (red), Gfap (green), and DAPI (blue). Cells at the center of the frame represent an astrocyte

841 (**A,** green arrowhead) or microglial cell (**B**, red arrowhead), respectively. (**C**) Orthogonal views of
842 an amoeboid microglial cell within the core of a lesion at 56 dpl. Scale bar: 25 μm.
843
844 **Supplemental Figure 3 (related to Methods). Significant post-operative weight loss in the**
845 **rabbit, and depiction of injection site.** (**A**) Dye injection (Evans Blue in PBS) showing injection
846 site (left hemisphere). Ruler, 1 mm between dashes. (**F**) Averaged weight of nonlesioned (blue)
847 and lesioned (gray) animals.

Figure 1

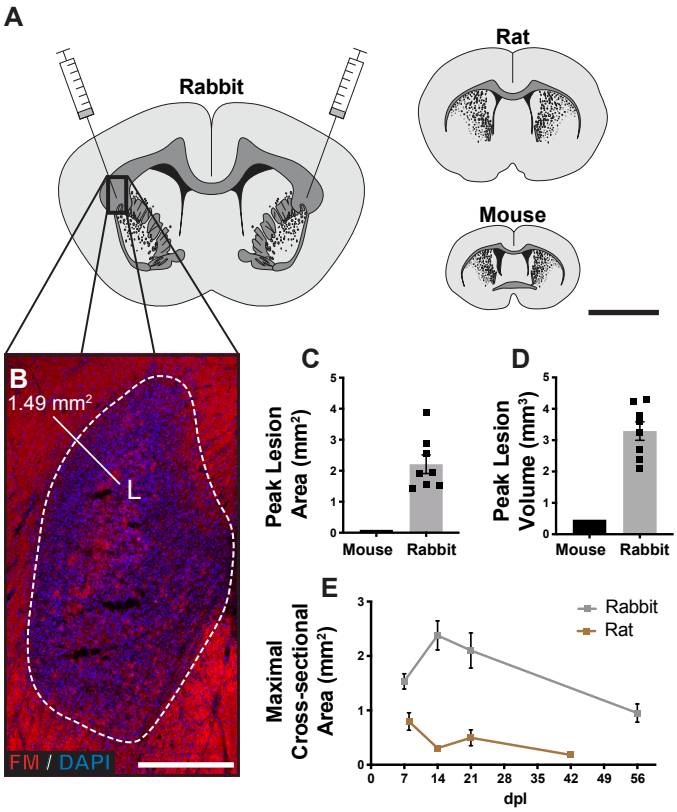
A
Rabbit
Rat
Mouse
B
1.49 mm²
L
FM / DAPI
C
Peak Lesion Area (mm²)
Mouse
Rabbit
D
Peak Lesion Volume (mm³)
Mouse
Rabbit
E
Maximal Cross-sectional Area (mm²)
Rabbit
Rat
dpl

Figure 2

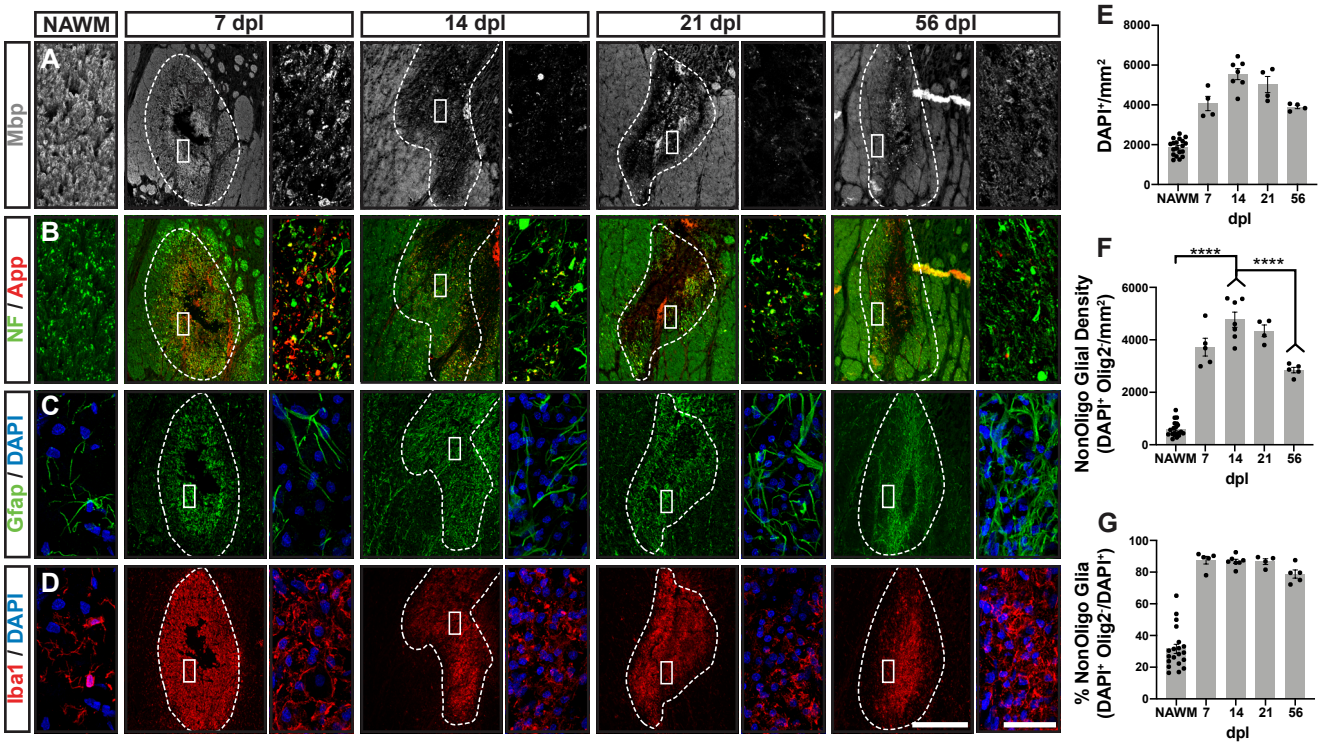
NAWM
7 dpl
14 dpl
21 dpl
56 dpl
Mbp
NF / App
Gfap / DAPI
Iba1 / DAPI
A
B
C
D
E
F
G
DAPI+/mm2
NonOligo Glial Density (DAPI+ Olig2-/mm2)
% NonOligo Glia (DAPI+ Olig2-/DAPI+)
dpl
****
****

Figure 3

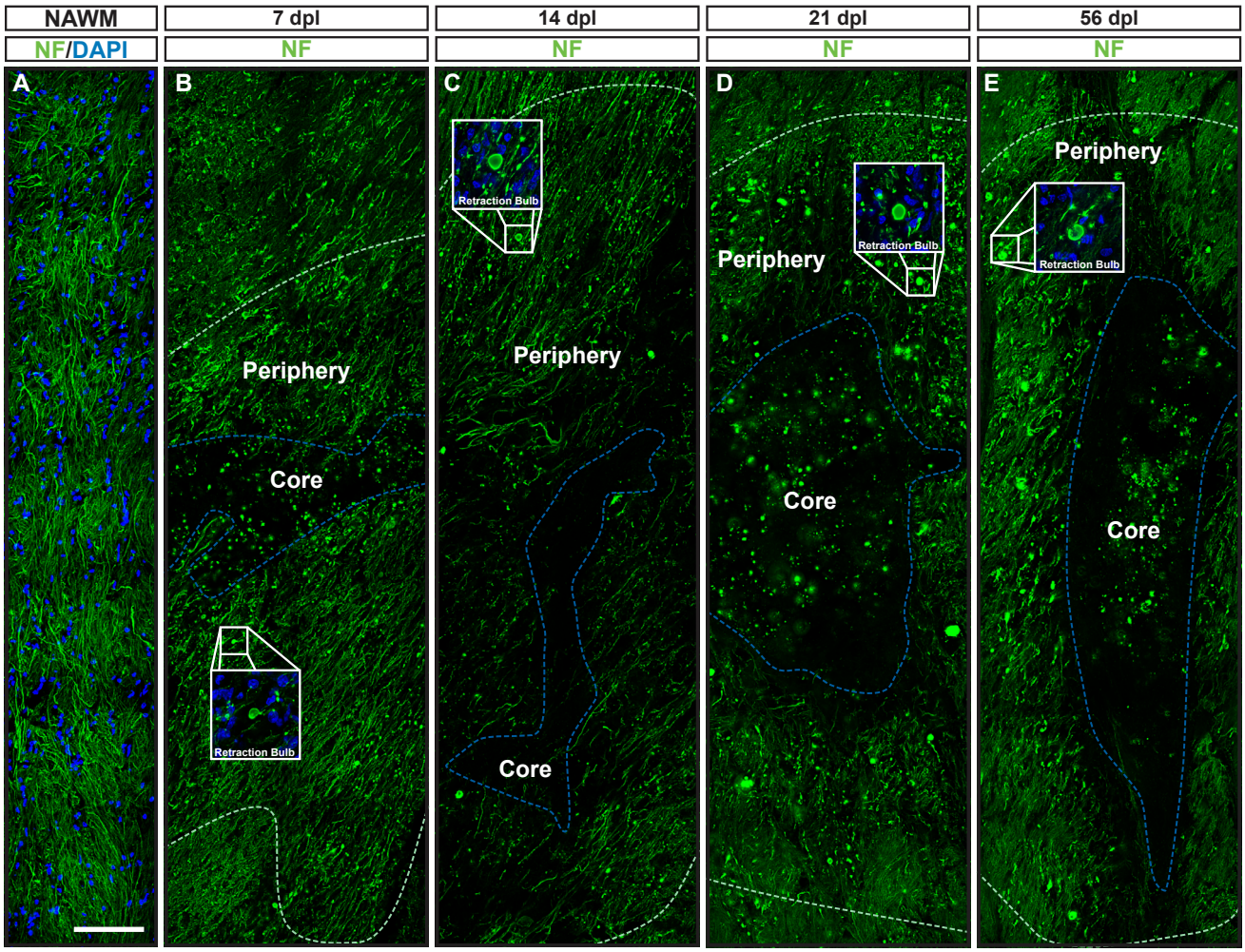
NAWM
7 dpl
14 dpl
21 dpl
56 dpl
NF/DAPI
NF
NF
NF
NF
A
B
C
D
E
Periphery
Core
Retraction Bulb
Periphery
Core
Retraction Bulb
Periphery
Core
Retraction Bulb
Periphery
Core
Retraction Bulb

Figure 4

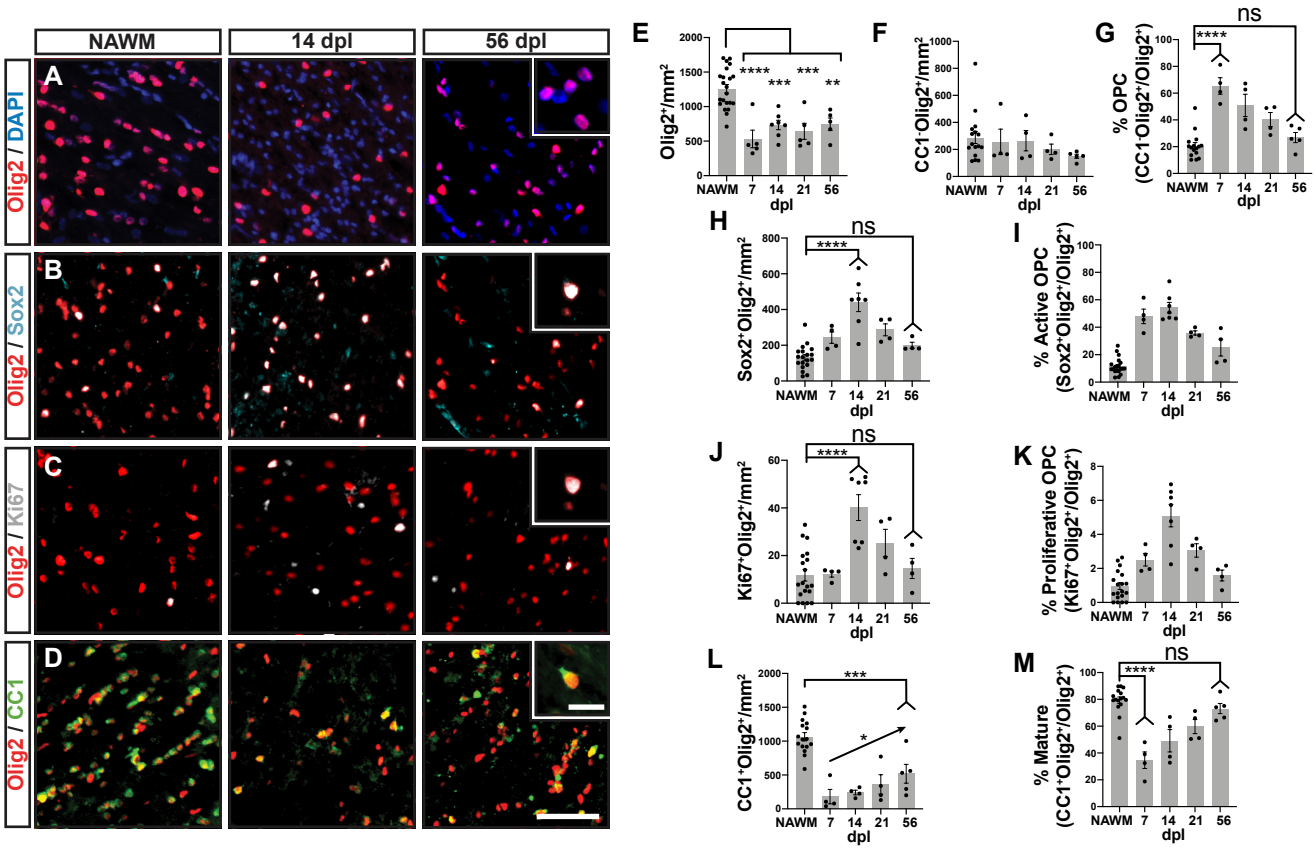
NAWM
14 dpl
56 dpl
A
Olig2 / DAPI
B
Olig2 / Sox2
C
Olig2 / Ki67
D
Olig2 / CC1
E
Olig2+/mm2
F
CC1-Olig2+/mm2
G
% OPC (CC1-Olig2+/Olig2+)
H
Sox2+Olig2+/mm2
I
% Active OPC (Sox2+Olig2+/Olig2+)
J
Ki67+Olig2+/mm2
K
% Proliferative OPC (Ki67+Olig2+/Olig2+)
L
CC1+Olig2+/mm2
M
% Mature (CC1+Olig2+/Olig2+)
NAWM 7 14 21 56
dpl
****
***
**
*
ns

Figure 5

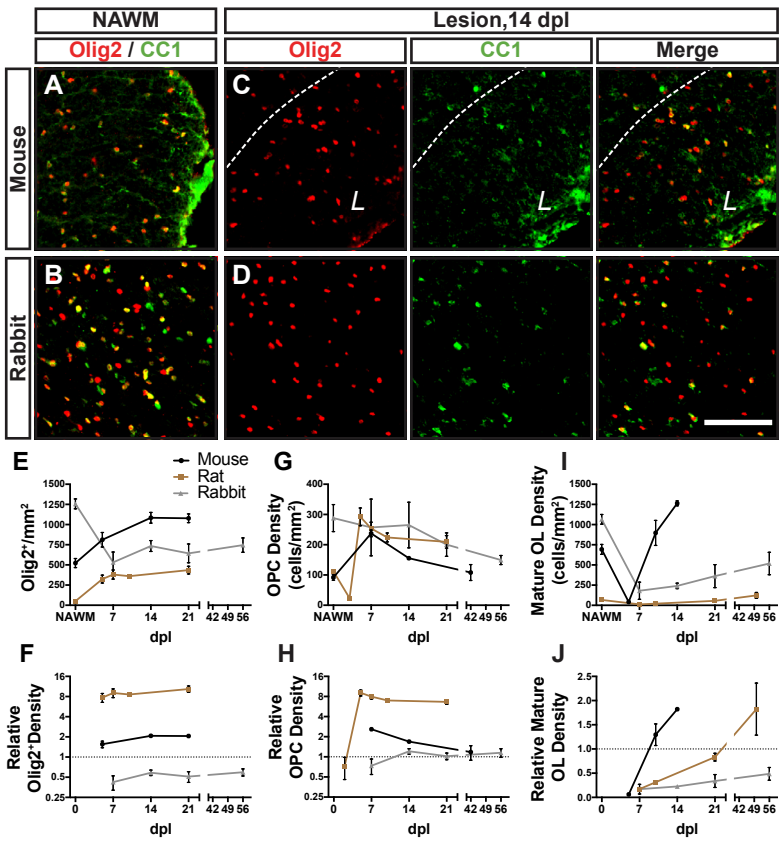
NAWM
Lesion,14 dpl
Olig2 / CC1
Olig2
CC1
Merge
Mouse
Rabbit
A
B
C
D
L
E
F
G
H
I
J
Mouse
Rat
Rabbit
Olig2+/mm2
Relative Olig2+Density
OPC Density (cells/mm2)
Relative OPC Density
Mature OL Density (cells/mm2)
Relative Mature OL Density
NAWM
dpl

Figure 6

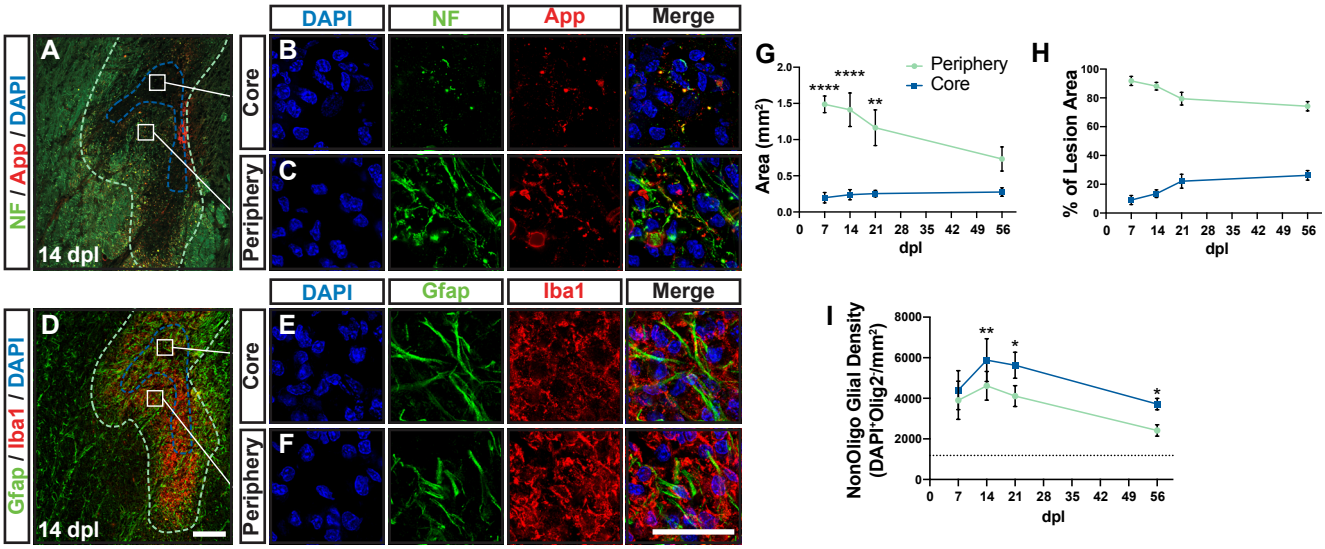
A
NF / App / DAPI
14 dpl
DAPI
NF
App
Merge
Core
Periphery
B
C
D
Gfap / Iba1 / DAPI
14 dpl
DAPI
Gfap
Iba1
Merge
E
F
G
Periphery
Core
Area (mm²)
dpl
H
% of Lesion Area
dpl
I
NonOligo Glial Density
(DAPI⁺Olig2⁻/mm²)
dpl

Figure 7

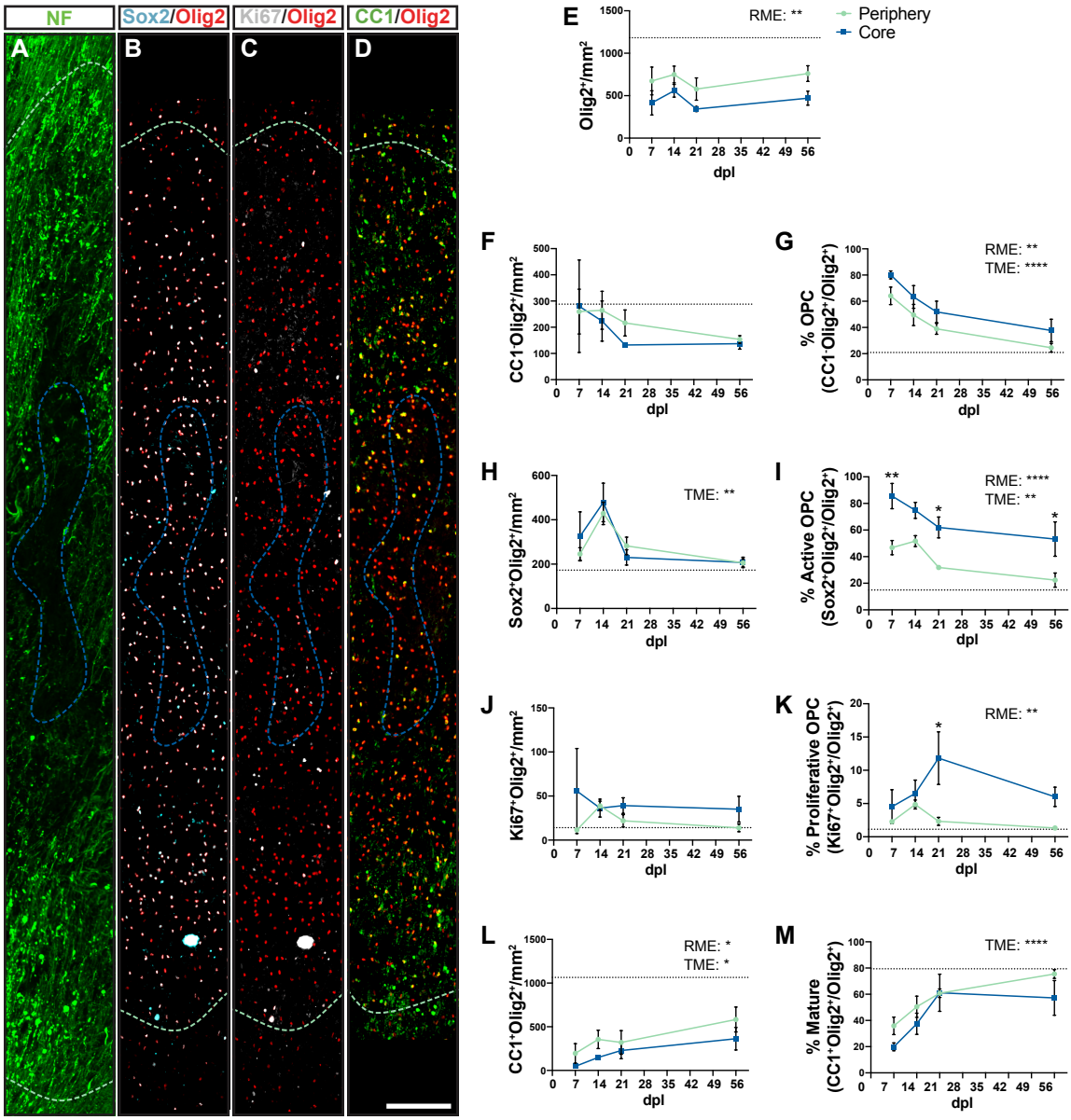
NF
Sox2/Olig2
Ki67/Olig2
CC1/Olig2
A
B
C
D
E
RME: **
Periphery
Core
Olig2+/mm2
dpl
F
CC1-Olig2+/mm2
G
RME: **
TME: ****
% OPC (CC1-Olig2+/Olig2+)
H
TME: **
Sox2+Olig2+/mm2
I
RME: ****
TME: **
% Active OPC (Sox2+Olig2+/Olig2+)
J
Ki67+Olig2+/mm2
K
RME: **
% Proliferative OPC (Ki67+Olig2+/Olig2+)
L
RME: *
TME: *
CC1+Olig2+/mm2
M
TME: ****
% Mature (CC1+Olig2+/Olig2+)

Figure 8

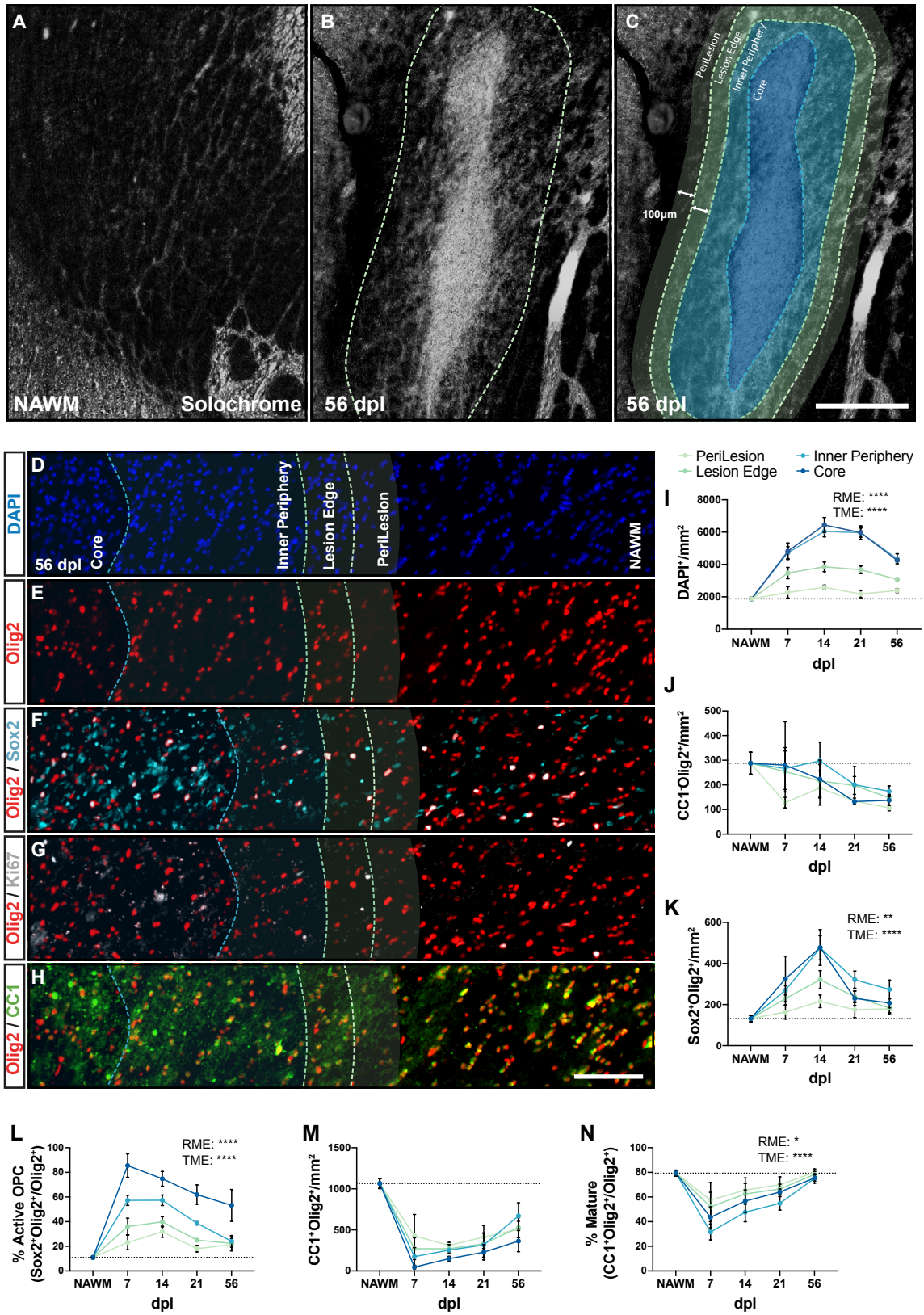
A
NAWM
Solochrome
B
56 dpl
C
56 dpl
PeriLesion
Lesion Edge
Inner Periphery
Core
100µm
D
DAPI
56 dpl
Core
Inner Periphery
Lesion Edge
PeriLesion
NAWM
E
Olig2
F
Olig2 / Sox2
G
Olig2 / Ki67
H
Olig2 / CC1
PeriLesion
Lesion Edge
Inner Periphery
Core
I
RME: ****
TME: ****
DAPI+/mm2
NAWM 7 14 21 56
dpl
J
CC1+Olig2+/mm2
NAWM 7 14 21 56
dpl
K
RME: **
TME: ****
Sox2+Olig2+/mm2
NAWM 7 14 21 56
dpl

L
RME: ****
TME: ****
% Active OPC
(Sox2+Olig2+/Olig2+)
NAWM 7 14 21 56
dpl
M
CC1+Olig2+/mm2
NAWM 7 14 21 56
dpl
N
RME: *
TME: ****
% Mature
(CC1+Olig2+/Olig2+)
NAWM 7 14 21 56
dpl

Supplemental 1

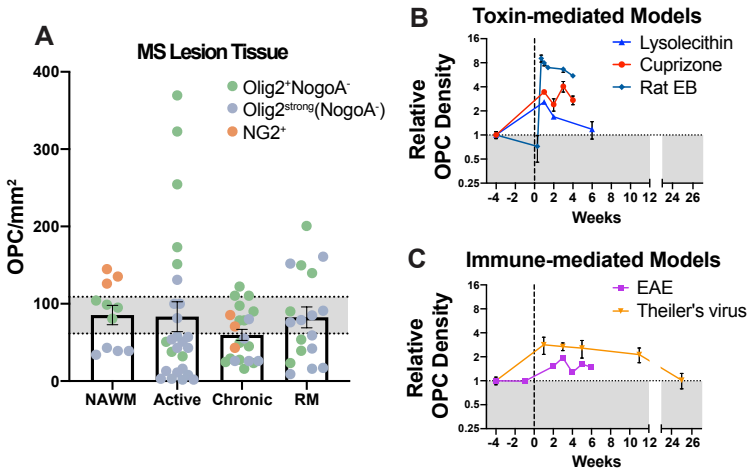

Supplemental 3

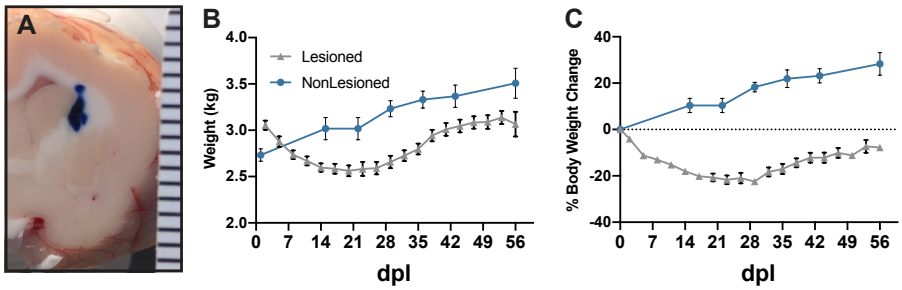
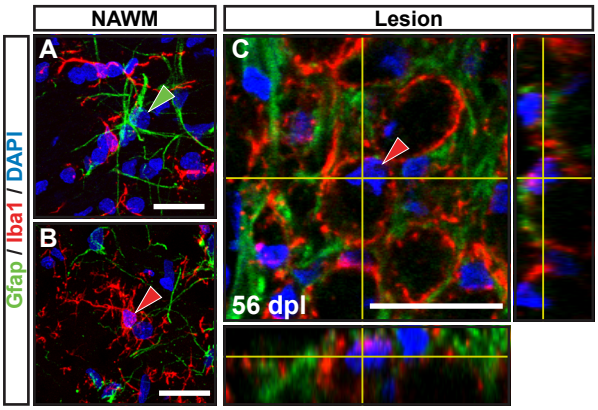
Supplemental 2